Geophysical Journal International

Geophys. J. Int. (2021) **226,** 1432–1460
Advance Access publication 2021 March 18
GJI Geodynamics and Tectonics

doi: 10.1093/gji/ggab108

Global mantle flow retrodictions for the early Cenozoic using an adjoint method: evolving dynamic topographies, deep mantle structures, flow trajectories and sublithospheric stresses

S. Ghelichkhan [1], H.-P. Bunge [2] and J. Oeser[2]

[1]*Research School of Earth Sciences, Australian National University, Canberra, ACT* 0200, *Australia. E-mail: siavash.ghelichkhan@anu.edu.au*
[2]*Department of Earth and Environmental Sciences, University of Munich,* 80333 *Munich, Germany*

Accepted 2021 March 9. Received 2021 February 22; in original form 2020 November 18

SUMMARY

During the Cenozoic, the Earth experienced multiple first-order geological events that are likely mantle flow related. These include the termination of large-scale marine inundation in North America in the Palaeocene, the late Tertiary rise of Africa relative to other continents and the long-wavelength tilting of Australia since the late Cretaceous, which occurred when the continent approached the southeast Asia subduction systems on its northward passage from Antartica. Here we explore a suite of eight high-resolution, compressible, global mantle flow retrodictions going back to 50 Ma, using an adoint method with ≈670 million finite elements. These retrodictions show for the first time that these events emerge jointly as part of global Cenozoic mantle flow histories. Our retrodictions involve the dynamic effects from an upper mantle low-viscosity zone, assimilate a past plate-motion model for the tangential surface velocity field, probe the influence of two different present-day mantle state estimates derived from seismic tomography, and acknowledge the rheological uncertainties of dynamic Earth models by taking in four different realizations for the radial mantle viscosity profile, two of which were published previously. We find the retrodicted mantle flow histories are sensitive to the present-day mantle state estimate and the rheological properties of the Earth model, meaning that this input information is testable with inferences gleaned from the geological record. For a deep mantle viscosity of 1.7×10^{22} Pa s and a purely thermal interpretation of seismic structure, lower mantle flow velocities exceed 7 cm yr^{-1} in some regions, meaning they are difficult to reconcile with the existence of a hotspot reference frame. Conversely, a deep mantle viscosity of 10^{23} Pa s yields modest flow velocities (< 3 cm yr^{-1}) and stability of deep mantle heterogeneity for much of the retrodiction time, albeit at the expense that African uplift is delayed into the latest Neogene. Retrodictions allow one to track material back in time from any given sampling location, making them potentially useful, for example, to geochemical studies. Our results call for improved estimates on non-isostatic vertical motion of the Earth's surface—provided, for instance, by basin analysis, seismic stratigraphy, landform studies, thermochronological data or the sedimentation record—to constrain the recent mantle flow history and suggest that mantle flow retrodictions may yield synergies across different Earth science disciplines.

Key words: Mantle processes; Inverse theory; Numerical modelling; Dynamics: convection currents, and mantle plumes.

1 INTRODUCTION

Mantle convection is the main driving force for large-scale tectonic activity of our planet, and plate tectonics is its surface expression (Davies & Richards 1992). Current plate motions are well mapped (DeMets *et al.* 2010). But the rules of plate tectonics (Morgan 1968) allow one to reconstruct histories of plate motions. Initially established for the Cenozoic (Gordon & Jurdy 1986), global plate motion histories are now available for earlier times going back to the Mesozoic (e.g. Müller *et al.* 2016). This has made it possible to connect the recent plate tectonic evolution of our planet explicitly to other elements of the Earth system, such as sea-level fluctuations related to changes in ocean basin volumes (Müller *et al.* 2008).

The rules of mantle convection are physical laws in the form of conservation equations for mass, momentum and energy (Jarvis & McKenzie 1980). They govern the flow evolution and allow one to construct mantle flow histories by retrodicting (i.e. making 'predictions' about the past) earlier mantle states. This approach was done initially through backward advection schemes (Steinberger & O'Connell 1997), where one integrates model heterogeneity back in time from the present day by reversing the time step of the energy equation and ignoring thermal diffusion effects. That simple approach has paved the way for a formal inverse problem based on the adjoint method, with so-called adjoint equations providing sensitivity information in a geodynamic model relative to earlier system states. Adjoint equations have been derived for incompressible (Bunge *et al.* 2003; Ismail-Zadeh *et al.* 2004; Horbach *et al.* 2014), compressible (Ghelichkhan & Bunge 2016) and thermochemical (Ghelichkhan & Bunge 2018) mantle flow. There are also reports on savings in computational costs of the adjoint method by optimizing the step sizes (Price & Davies 2018), on using a hybrid forward-adjoint scheme (Zhou & Liu 2017), on simultaneous recoveries of initial temperature condition and rheology (Li *et al.* 2017) and on multiphysics adjoint modelling (Reuber & Simons 2020).

Mantle convection is a chaotic process. This seemingly rules out any construction of robust flow time trajectories (Bello *et al.* 2014). But the chaotic nature of mantle convection is overcome if one assimilates the horizontal surface velocity field (Colli *et al.* 2015). Knowledge of the latter is therefore essential to assure convergence (Vynnytska & Bunge 2014) of the inverse problem and to obtain a small null space for the restored flow evolution (Horbach *et al.* 2014). It makes past plate motions—in the form of plate motion histories—the input of retrodictions rather than their output and suggests that viable tests of mantle flow retrodictions should be linked to inferences of vertical lithosphere motion induced by mantle convective stresses. To this end geodynamicists have long known that convective stresses deflect the Earth's surface away from its isostatically compensated state (Pekeris 1935). Termed *dynamic topography* by Hager *et al.* (1985), the deflections have received renewed attention (e.g. Braun 2010; Hoggard *et al.* 2016; Davies *et al.* 2019; Valentine & Davies 2020), particularly in passive margin environments (Bunge & Glasmacher 2018) where the proximity to a base-level allows one to gauge topographic changes more robustly than at other places.

There has been much improvement in the amount and quality of dynamic topography inferences in recent years. Information on the present-day scale and amplitude of topography in convective support comes from studies of oceanic residual depth (Hoggard *et al.* 2017). Moreover a variety of geological indicators provide constraints on the temporal evolution of dynamic topography. They include studies of river profiles (e.g. Roberts & White 2010), sediment compaction (Japsen 2018) and provenance (Meinhold 2010; Şengör 2001), landform analysis (Guillocheau *et al.* 2018) based on planation surfaces (King 1955), estimates of palaeoaltimetry (Kohn 2007), constraints from thermochronological data (Ehlers & Farley 2003) or quantifications of sediment budgets at the scale of continental margins (Guillocheau *et al.* 2012; Said *et al.* 2015a, b). Further inferences are drawn from geological hiatus maps (Friedrich *et al.* 2018; Vibe *et al.* 2018; Hayek *et al.* 2020), palaeobiological and palaeoenvironmental data (Fernandes & Roberts 2020), past sea-level markers (DiCaprio *et al.* 2009; Matthews *et al.* 2011; Stephenson *et al.* 2019) or sequence stratigraphy (Czarnota *et al.* 2013; Richards *et al.* 2016; Hartley *et al.* 2011). A recent review on observations of dynamic topography through space and time is given by Hoggard *et al.* (2021).

From the above it is clear that our theoretical understanding of mantle flow retrodictions has progressed significantly, and that geodynamically relevant constraints on dynamic topography and its temporal evolution have grown. However, one must state clearly that the accuracy of any mantle flow restoration depends on the error associated with the three essential information sources for the inverse problem, that is the geodynamic model, the state estimate of mantle heterogeneity and the assimilated history of horizontal surface velocities. The mantle flow conservation equations are not in question, but significant uncertainty exists in the choice of key geodynamic modelling parameters, such as mantle rheology and composition. The state estimate of present-day mantle heterogeneity is also subject to substantial uncertainty owing to the finite resolution of seismic tomography, as seen from synthetic experiments where one constructs tomographic images from geodynamic input structures (e.g. Mégnin *et al.* 1997; Bunge & Davies 2001). Different tomographic models are currently in agreement only over length-scales of thousands of kilometres (Becker & Boschi 2002; Debayle & Ricard 2012) and tend to disagree at smaller scales, implying that dynamically significant mantle heterogeneity features may either be poorly resolved or missed completely (Schuberth *et al.* 2009a). Plate reconstructions also become less reliable when moving progressively back in time (Rowan & Rowley 2017) and involve choices of absolute reference frames that lead to considerable uncertainty in their link to mantle flow (Shephard *et al.* 2012). The difficulty of constraining past plate motion is particularly severe for plates completely surrounded by subduction zones (e.g. Wu *et al.* 2016), although new slab unfolding techniques may help reconstruct now-subducted plates using tomographic images of slabs in the mantle (Wu & Suppe 2018).

Despite inevitable uncertainties in our information sources for the inverse problem of mantle flow retrodiction, there exist some first-order geological events in the Cenozoic that are likely mantle flow related. They offer opportunities for geodynamicists to assess the performance of global mantle flow retrodictions. A prominent example is the termination of large-scale marine inundation in North America at the end of the Cretaceous and early Palaeogene, which has been linked to the waning influence of the sinking Farallon slab causing dynamic rebound (e.g. Mitrovica *et al.* 1989; Burgess *et al.* 1997). Another is the late Tertiary rise of Africa relative to other continents (Bond 1978). Pointed out by Krenkel (1924) nearly 100 yr ago, Africa's topographic growth has been documented by many authors (e.g. Bond 1978; Şengör 2001; Carena *et al.* 2019) and reviewed thoroughly by Burke & Gunnell (2008), such that it is now widely agreed that the Oligocene was a period of uplift throughout most of the continent. A third example involves long-wavelength tilting of Australia since the late Cretaceous (Sandiford 2007; DiCaprio *et al.* 2009), which occurred when the continent approached the subduction systems in southeast Asia on its northward passage. Reports suggest that the tilting coincided with regional uplift of the eastern Australian highlands (Czarnota *et al.* 2014).

Until now, the adjoint method has been applied to reconstruct mantle convection histories in global settings, but with the analysis confined to regional studies in the Americas (Liu & Gurnis 2010; Shephard *et al.* 2010; Spasojevic *et al.* 2009; Liu *et al.* 2008) and the Atlantic

realm (Colli *et al.* 2018). Restricted by computational expense, these studies limited themselves in their exploration of the parameter space, that is seismic tomographic input models and assumed mantle viscosity structures. To account more broadly for model parameter space and to gain improved assessments of the retrodictions, we take a different approach. We build upon our previous work in Colli *et al.* (2018) and explore a suite of eight global retrodiction models (called RM from here on) for the past 50 Myr. We use two recent whole-mantle tomographic models by Simmons *et al.* (2015) and French & Romanowicz (2014), combined with the upper mantle shear wave speed model of Schaeffer & Lebedev (2013). We also examine four different mantle viscosity profiles. These include two published viscosity profiles of Mitrovica & Forte (2004) and Steinberger & Calderwood (2006) next to two viscosity profiles that we inverted optimally for the gravitational potential shape of the Earth. Conversion of seismic velocities to flow-driving mantle buoyancies are performed by using the thermodynamically self-consistent mantle mineralogy model of Stixrude & Lithgow-Bertelloni (2011) together with an anelasticity model of the mantle (Cammarano *et al.* 2003) to account for the non-linearity in mappings of seismic shear speed to temperature and density. We organize our paper as follows: Section 2 lists the methodologies used for this study. Here we specify forward and adjoint mantle convection equations, the numerical modelling code, our assumptions for the misfit function, estimates of present-day mantle heterogeneity, choices for radial viscosity profiles, as well as the dynamic topography calculations. Next, we report results in Section 3. We start by providing metrics of optimization in the eight retrodiction models. This is followed by showing retrodictions of dynamic topographies, deep mantle structures and flow fields together with trajectories of upper mantle material transport beneath Europe for four end-member models. Finally, we focus on one particular model to explore regional patterns, for which we present the evolving upper mantle flow field beneath Europe and the central Pacific, the evolving upper mantle stress field beneath Australia, North America and Africa and mantle heterogeneity cross sections beneath North America and Africa, to display the time dependent nature of the sinking Farallon Plate and the rising Afar plume structure. We end our paper with a discussion in Section 4 and draw some conclusions in Section 5.

2 METHOD

2.1 Mantle convection forward and inverse problem

The forward mantle convection equations embody conservation principles for mass, momentum and energy. We solve them in the anelastic-liquid approximation (Jarvis & McKenzie 1980) using the finite-element mantle convection code TERRA (Bunge & Baumgardner (1995); see Davies *et al.* (2013) for discretization characteristics and benchmarks) for the time interval $[t_I,\ t_F]$, with t_I and t_F representing times at, respectively, 50 Ma and present-day, within a spherical shell V (i.e. the Earth's mantle) with boundary $\partial V = S \cap C$, with S denoting the Earth's surface and C the core–mantle boundary (CMB),

$$\nabla \cdot (\rho_r \mathbf{v}) = 0, \tag{1a}$$

$$\nabla \cdot \left[\eta \left(\nabla \mathbf{v} + (\nabla \mathbf{v})^T - \frac{2}{3} (\nabla \cdot \mathbf{v}) \mathbb{I} \right) \right] - \nabla p + \alpha \rho_r g \, (T_{av} - T) = 0, \tag{1b}$$

$$\partial_t T + \gamma T \nabla \cdot \mathbf{v} + \mathbf{v} \cdot \nabla T - \frac{1}{\rho_r c_v} [\nabla \cdot (k \nabla T) + \tau : \nabla \mathbf{v}] + H = 0. \tag{1c}$$

The three unknowns in eq. (1) are velocity, $\mathbf{v}$, pressure, p and temperature, T. The first term in parentheses in eq. (1b) is equal to the deviatoric strain-rate tensor, which has a linear relationship with the deviatoric stress tensor, τ, in eq. (1c). $\mathbb{I}$ is the unit tensor. Table 1 lists the parameters in eqs. (1) with the definitions and their corresponding values used in this study. Our high resolution mesh discretizes Earth's mantle with ≈670 million finite element nodes. This value corresponds to a grid point resolution of 11 km radially, and 14 km tangentially at the surface, decreasing to half that value at the CMB and allows one to resolve global mantle flow at Earth-like convective vigor. Calculations are performed on 2048 computational cores of the SuperMUC facility at the Leibniz Supercomputing Centre (LRZ) in Munich (Germany) and

Table 1. Parameters used in all retrodiction models.

Parameter	Symbol	Value	Unit
Radial density profile	ρ_r	PREM	$\mathrm{kg\,m^{-3}}$
Average mantle density	$\Delta\overline{\rho}$	4500	$\mathrm{kg\,m^{-3}}$
Gravitational acceleration	g	Calculated self-consistently with ρ_r	$\mathrm{m\,s^{-2}}$
Viscosity	η	see Fig. 3	$\mathrm{Pa \cdot s}$
Radial average temperature profile	T_{av}		K
Temperature boundary condition	T (surface)	300	K
	T (CMB)	4200	K
Grüneisen parameter	γ	1.1	
Specific heat capacity at constant volume	c_v	1000	$\mathrm{J\,kg^{-1}K^{-1}}$
Thermal expansivity	α (surface)	3.3×10^{-5}	$\mathrm{K^{-1}}$
	α (CMB)	1.2×10^{-5}	$\mathrm{K^{-1}}$
Thermal conductivity	k	2.5	$\mathrm{W\,m^{-1}K^{-1}}$
Specific radiogenic heat production rate	H	0.5×10^{-11}	$\mathrm{W\,m^{-3}}$

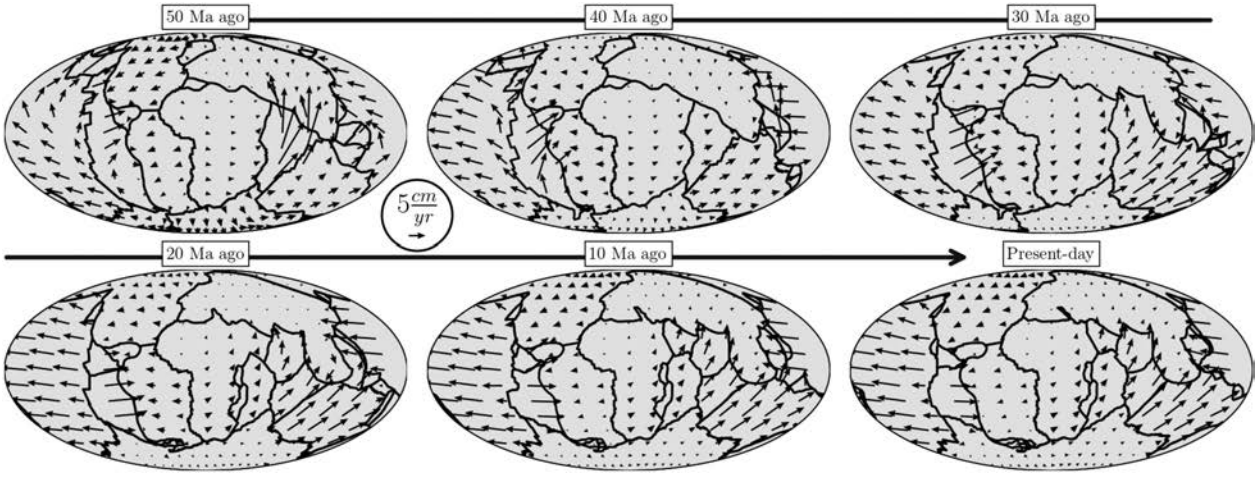

Figure 1. Surface velocities obtained from the Cenozoic Plate reconstruction model of Müller *et al.* (2016) within a moving hotspot reference frame (Torsvik *et al.* 2008) as included in Young *et al.* (2019). We map the velocity vectors onto the TERRA grid using GPlates software (Müller *et al.* 2018) with a temporal resolution of 1 Ma, with smoothed velocities within one degree of plate boundaries.

a local computer cluster dedicated to capacity geophysical modelling (Oeser *et al.* 2006). The forward problem in eqs. (1) must be supplied with boundary conditions. For the energy equation, we apply Dirichlet (prescribed function value for temperature) boundary conditions as described in Table 1. For the momentum balance, we impose a free-slip (i.e. zero tangential stresses) boundary condition at the CMB. At the top surface, we apply a time-dependent Dirichlet (i.e. prescribed velocities) boundary condition as described by Bunge *et al.* (1998), obtained from the plate motion history model of Müller *et al.* (2016) as included in Young *et al.* (2019). The latter is converted to velocity vectors on the TERRA grid using GPlates software (Müller *et al.* 2018) with a temporal resolution of 1 Ma, with smoothed velocities within one degree of plate boundaries. Fig. 1 is the visualization of prescribed surface velocities along with the reconstructed plate boundaries in Young *et al.* (2019) for 10 Myr intervals .

We reconstruct a past mantle state at $t = t_I = 50$ Ma by minimising a misfit functional. It measures the difference between computed model temperature and the 'observed' mantle temperature field at present-day. The latter is obtained by mapping seismic tomographic structure to temperature, followed by the use of thermodynamic relationships between seismic wave speed, temperature and pressure for mantle minerals. Owing to the finite resolution of seismic tomography, the retrieval of wave speed structure in global tomographic models occurs on coarser scales compared to the high resolution geodynamic model used in this study (≈11 km). To avoid artefacts, we follow Colli *et al.* (2018, 2020) and account in the misfit functional for the resolution difference between model predictions and the present-day state estimate. To this end, we define the misfit functional with a low-pass filtering of fields as

$$\tilde{F}(r,\theta,\phi) = \sum_{l=0}^{lmax}\sum_{m=-l}^{m=+l} G_r(r) * G_l \left(\int_0^{2\pi}\int_0^{\pi} F(r,\theta,\phi)\, Y_{lm}(\theta,\phi)\, \sin(\theta)\, \mathrm{d}\phi\, \mathrm{d}\theta \right) Y_{lm}(\theta,\phi). \tag{2}$$

In eq. (2), $*$ represents convolution, $\tilde{F}$ is the result of filtering on a scalar 3-D field F, Y_{lm} are spherical harmonic (SH) functions, $lmax = 50$ is the maximum SH degree, G_r a normalized Gaussian function with a half-width of ≈50 km, G_l is 1 for all spherical harmonics smaller than SH degree 35, and tapers to zero at degree 50 with a Gaussian radius of 8. In plain terms, eq. (2) describes in order, a SH transformation of the spatial field, a low-pass filter of SH coefficients at each layer, a radial Gaussian smoothing of the SH coefficients at each l and m, and a back-transformation to the spatial domain. Fig. A1 reports the lateral and radial filtering parameters and functions in eq. (2). The misfit functional is subsequently defined as

$$\chi = \int_V \frac{1}{2}\left(\tilde{T}(t = t_F) - \tilde{T}_E\right)^2 \mathrm{d}x, \tag{3}$$

where $\tilde{T}$ and $\tilde{T}_E$ are, respectively, the filtered model and reference temperature fields at present-day. The misfit functional in eq. (3) is the L_2 norm of the difference between model temperature at time t_F, and the reference temperature for the mantle. It can be shown (Ghelichkhan & Bunge 2016) that the derivative of the misfit function w.r.t. the initial temperature field is $\Psi(t = t_I)$, which is obtained by solving the coupled equations of

$$\nabla \cdot \phi = 0, \tag{4a}$$

$$\nabla \cdot \left[\eta\left(\nabla\phi + (\nabla\phi)^T\right)\right] + \Psi\nabla T - \rho_r \nabla\lambda - 2\nabla\cdot\left(\tfrac{\Psi}{\rho_r c_v}\tau\right) = 0, \tag{4b}$$

$$\partial_t \Psi + v\cdot\nabla\Psi - (\gamma - 1)\Psi\nabla\cdot v + \nabla\cdot\left(k\nabla\left(\tfrac{\Psi}{\rho_r c_v}\right)\right) + \alpha\rho_r g\cdot\phi = \tilde{T}(t_F) - \tilde{T}_E, \tag{4c}$$

where Ψ, ϕ and λ are, respectively, the adjoint temperature, velocity and pressure fields. A gradient method of choice, for example steepest descent or conjugate gradient, can be supplied with the gradient information to minimize χ and consequently restore past mantle states. However, these methods often use a line search approach to determine the optimization step-size (amplitude of the step in the opposite direction of the gradient), which translates into multiple forward and adjoint calculations per iteration. To circumvent the excess numerical expense associated with the line-search, we use a heuristic approach, similar to backtracking line-search methods. We initialize the step-size with 0.4 (dimensionless), and subsequently reduce it by 0.1 after every five iterations. These values are based on published synthetic numerical experiments (Ghelichkhan & Bunge 2016, 2018) and are in general agreement with previous studies (Ismail-Zadeh *et al.* 2004; Price & Davies 2018).

We recall that in the presence of data and model uncertainties, it is not desirable to aim for a complete reduction of the misfit function, as it results in overfitting of the model (Colli *et al.* 2020). In general, one avoids overfitting by imposing additional constraints on the optimization problem. This may be enforced explicitly, for example by augmenting the misfit function as in Tikhonov regularization (Tikhonov 1963), or implicitly, for example by choosing a large convergence tolerance for the minimization problem. Here we use an implicit approach by an *early-stopping criterion* of the minimization, where results are analysed for that iteration where the misfit function begins to flatten. Thus all retrodictions are presented after five iterations.

2.2 Present-day mantle state estimates

2.2.1 Seismic imaging

We take advantage of simultaneous progress in whole mantle and upper mantle seismic tomography. Our representation of uppermost mantle (i.e. shallower than 400 km) structure relies on the vertically polarized shear speed model SL2013sv (Schaeffer & Lebedev 2013), which yields considerable improvements in resolution of uppermost mantle features (globally up to $\approx$ 300 km, regionally higher). At each depth, the vertical wave speed is converted to the Voigt average isotropic speed (see Appendix in Panning & Romanowicz 2006, for a derivation)

$$V_s = \sqrt{\frac{2V_{sv}^2 + V_{sh}^2}{3}} = \sqrt{\frac{2V_{sv}^2 + (\xi(r)\, V_{sv})^2}{3}}, \tag{5}$$

where ξ is the horizontal to vertical shear speed ratio profile in PREM (Dziewonski & Anderson 1981). For depths larger than 400 km, we use two global tomographic models. One is the shear wave speed model LLNL-G3D-JPS (Simmons *et al.* 2015), which is constructed from a joint inversion of shear and compressional wave travel times for $\approx$ 3 million high-quality data. The other is the shear wave speed model SEMUCB-WM1 (French & Romanowicz 2014), obtained by a hybrid full-wave form inversion of a data set of $\approx$ 400 000 waveform windows. A radial smoothing in the filtering process of eq. (2) ensures a smooth transition into the lower mantle between SL2013sv and the deeper mantle models.

2.2.2 Seismic heterogeneity mapping to temperature and density through mineralogic models

Mantle mineralogy models (Piazzoni *et al.* 2007; Stixrude & Lithgow-Bertelloni 2011; Chust *et al.* 2017) allow mapping of seismic heterogeneity to thermal and density variations for a given mantle composition. The dependence on pressure translates directly to depth (Cammarano *et al.* 2005). But the temperature dependence is complicated by elastic (anharmonic) and anelastic effects. We obtain a look-up table for mantle minerals by assuming a homogeneous pyrolitic mantle (Ringwood 1991), consistent with the interpretation of a predominantly thermal origin for large-scale mantle seismic anomalies. The stable mineral phases are computed using the solution parameters compiled by Stixrude & Lithgow-Bertelloni (2011) in Perple_X software (Connolly 2005). Fig. 2(a) shows the shear wave speed variation as a function of depth and temperature.

In Fig. 2, one can observe sharp seismic velocity changes due to abrupt changes in phase proportions, which are distinct features of 1-D seismic reference models (e.g. Dziewonski & Anderson 1981; Kennett & Engdahl 1991). The non-zero Clapeyron slopes for mantle phase transitions imply thermally induced undulations (topography) along these transition zones. Seismologists use SS and PP precursors to globally map these undulations (Deuss 2009). Moreover, tomographic models—including LLNL-G3D-JPS—are beginning to incorporate them by allowing for explicit representation of undulating and discontinuous layers. But current uncertainties in seismic and mineralogical models imply a biased mapping of phase topography into unphysical temperature jumps in the transition zone. We mitigate such artefacts and linearize the look-up table by finding the median of $\frac{\mathrm{d}V_s}{\mathrm{d}(T,\rho)}$ around $\pm$500 K of average temperature and density profiles obtained from a recent mantle circulation model (Nerlich *et al.* 2016, dashed line in Fig. 2a) and PREM (Dziewonski & Anderson 1981). We also account for the attenuation of seismic waves, which at a given pressure, is a temperature dependent effect that introduces a non-linear wave speed sensitivity to temperature. We honor these non-linear effects with an updated version of the Q_5 model (Cammarano *et al.* 2003). This update is applied, because Cammarano *et al.* (2003) use an extrapolation of the upper mantle solidus *KLB1* (Hirschmann 2000) for lower mantle pressures. Q_5 in our study uses the KLB1 profile in the uppermost mantle (up to 10 GPa), with a linear transition to a lower mantle solidus by Andrault *et al.* (2011). Fig. 2(b) reports quality factor Q_5 at various temperatures and depths. Linearized elastic values are corrected for attenuation by

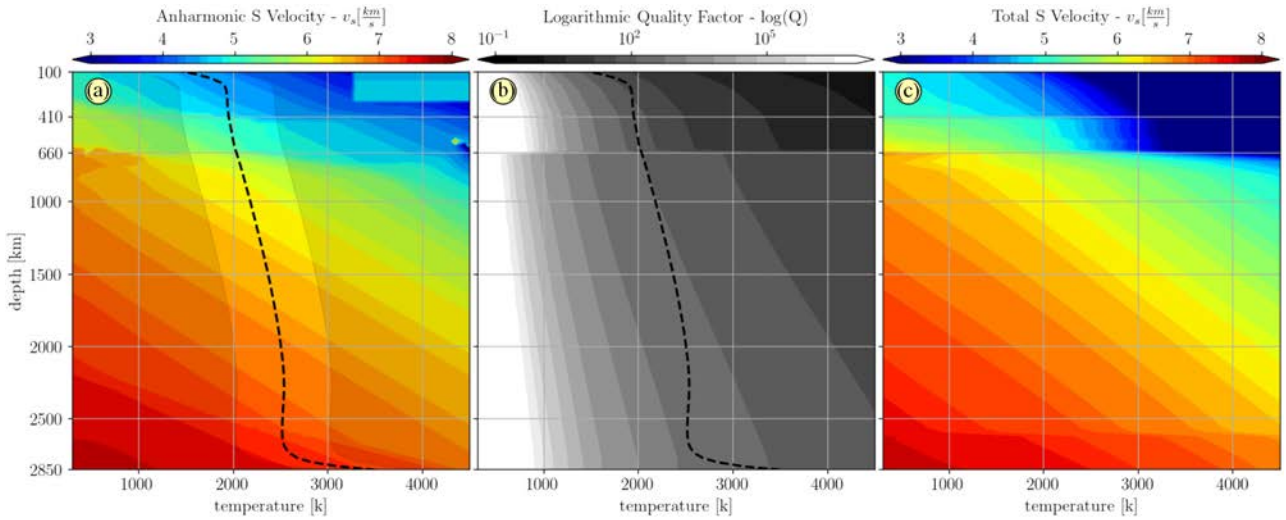

Figure 2. Mapping of seismic shear speed to temperature, (a) elastic shear speed as a function of depth (pressure) and temperature. The values are computed using stable mineral assemblage for pyrolitic mantle (Stixrude & Lithgow-Bertelloni 2011) in Perplex (Connolly 2005). The dashed line is the assumed geotherm profile, with ±500 presented as non-shaded area. We mitigate artifacts from phase transitions by linearizing the look-up table by finding the median of $\mathrm{d}V_s/\mathrm{d}(T, \rho)$ in the non-shaded area. Panel (b) an updated version of the Q_5 model (Cammarano *et al.* 2003) as a function of depth and temperature. The update is applied, because Cammarano *et al.* (2003) use an extrapolation of the upper mantle solidus *KLB1* (Hirschmann 2000) for lower mantle pressures. Q_5 in our study uses the KLB1 profile in the uppermost mantle (up to 10 GPa), with a linear transition to a lower mantle solidus by Andrault *et al.* (2011). Panel (c) resulting anelastic look-up table from a linearized version of (a) and anelastic effects using quality factor in (b), which allows us to map seismic anomalies to temperature and density.

using the low-attenuation limit approximation (Stixrude & Lithgow-Bertelloni 2005),

$$1 - \frac{V_s^{\omega}(P,T)}{V_s^{\infty}(P,T)} = \frac{1}{2}\cot\left(\frac{\alpha\pi}{2}\right) Q^{-1}(P,T). \tag{6}$$

where V_S^{ω} and V_S^{∞} are the anelastic and elastic shear speeds and α is the frequency exponent, with a value of 0.2 for Q_5 as reported by Cammarano *et al.* (2003). Fig. 2(c) shows the resulting anelastic look-up table that allows us to map seismic wave speeds to temperature. This yields two estimates of present-day mantle thermal and density heterogeneity corresponding to the two tomographic input structures used in this study: LSQ_5P and SSQ_5P obtained from combining SL2013sv either with LLNL-G3D-JPS or SEMUCB-WM1, respectively.

2.3 Input mantle viscosity profiles

The relationship between stress and strain-rate, that is viscosity, plays a crucial role in mantle flow retrodictions. Geoid and GIA studies (e.g. Richards & Hager 1984; Mitrovica 1996) show that the viscosity profile of the mantle reaches a minimum in the upper mantle. But there is a well-known trade off between the magnitude and depth range of this viscosity reduction (Paulson & Richards 2009; Schaber *et al.* 2009). We address this uncertainty by using four different viscosity profiles, including two published profiles, MF-2004 (Mitrovica & Forte 2004) and SC-2006 (Steinberger & Calderwood 2006), and two profiles that are self-consistently inverted in this study. MF-2004 (yellow profile in Fig. 3-I) is derived from a joint inversion of observations related to mantle convection and ice age dynamics. It has a three orders of magnitude increase in viscosity from the shallow mantle to 2000 km depth, followed by a reduction of comparable magnitude toward the CMB. SC-2006 (red profile in Fig. 3-I) fits mineralogical parameters of activation energy to geoid constraints. It consists of a low viscosity channel with a sharp transition to the lower mantle at 660 km, followed by an increase to 10^{23} Pa s at ≈ 2200 km depth, with a four orders of magnitude reduction between 2500 km depth and the CMB. Both profiles are obtained from inversions for a mantle heterogeneity structure that differs from the ones we used in this study. We mitigate this inconsistency by constructing an additional viscosity profile optimised for the heterogeneity models used in our study. To this end, we invert for the long-wavelength geoid using a *direction set method in multidimensions* (Press *et al.* 1992) and find an optimal viscosity profile by minimizing the misfit function

$$\mathfrak{M} = 1 - (0.9 \times \mathrm{Corr}_{\mathrm{geoid}} + 0.1 \times \mathrm{Corr}_{\mathrm{CMB}}), \tag{7}$$

where $\mathrm{Corr}_{\mathrm{geoid}}$ and $\mathrm{Corr}_{\mathrm{CMB}}$ are correlation coefficients between long wavelength (up to SH degree 7) modelled and observed geoid and CMB dynamic topography, respectively. For the observed geoid and CMB observations, we use the satellite gravity field model *GOCO05s* (Pail *et al.* 2010), corrected for the hydrostatic shape of the Earth (Nakiboglu 1982) and the CMB topography model of Koelemeijer *et al.* (2017), respectively. The correlation coefficient for CMB topography is added to increase sensitivity in the deep mantle, albeit with a 1 to 9 weighting, to acknowledge the high uncertainties in CMB topography models. A Haskell constraint is imposed for the volumetric integral of viscosities in the upper 1000 km (Haskell 1935; Mitrovica 1996), as geoid inversions are insensitive to absolute viscosity values. For the sake of simplicity, we parametrize the viscosity profile with three values (i.e. number of unknowns $n = 3$), representing viscosities in the asthenosphere, the

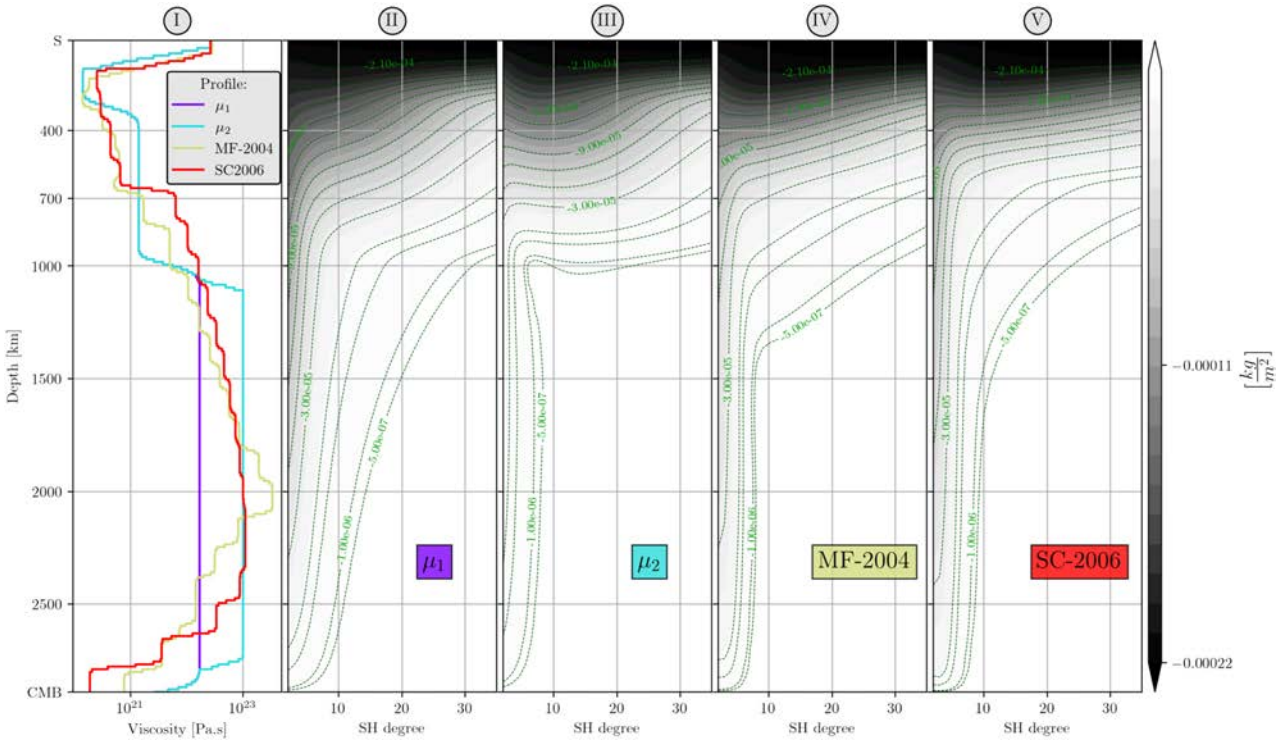

Figure 3. (I) Viscosity profiles used in this study: MF-2004 (Mitrovica & Forte 2004), is derived from a joint inversion of data related to mantle convection and ice age dynamics, and is characterized by a three order of magnitude increase in viscosity from the shallow mantle to 2000 km depth, followed by a reduction of comparable magnitude towards the core–mantle boundary. SC-2006 (Steinberger & Calderwood 2006), is obtained mainly by fitting mineralogical parameters of activation energy and constrained by observations of gravitational field of Earth. μ_1 is obtained by inverting for geodetic and seismic observations (see text). μ_2 is similar to μ_1, except for an increased viscosity in the lower mantle starting from $\approx$ 1100 km. This profile is mainly to address the uncertainties regarding lower mantle values. (II, III, IV and V) Dynamic topography kernels in 2-D representation (see Colli *et al.* 2016) calculated for the four viscosity profiles of μ_1, μ_2 MF-2004 and SC-2006, respectively. In models with weak asthenospheric layer, lower mantle contribution to dynamic topography is restricted to long wavelength (up to SH degree 5) anomalies. For μ_2, where there is an almost two orders of magnitude contrast between mid-mantle and lower mantle, the contribution from lower mantle is significantly lower. Kernels for more sophisticated profiles of MF-2004 and SC-2006 show an intermediate partitioning of lower mantle to upper mantle when compared to μ_1 and μ_2.

upper mantle below the asthenosphere (at 400-1000 km) and the deeper mantle (1000-2890 km). Our choice for these depth levels is supported by, among others, two constraints: first, are observational and modelling studies of an asthenosphere channel accommodating faster than observed plate velocities (e.g. Hartley *et al.* 2011; Colli *et al.* 2014; Weismüller *et al.* 2015). This hints at a weak asthenosphere. Secondly, are studies that associate the ≈1000 km depth level with a sharp viscosity increase (Ballmer *et al.* 2015; Rudolph *et al.* 2015). We also impose a two orders of magnitude viscosity increase in the uppermost 50 km and decrease in the lowermost 30 km above the CMB to represent, respectively, the effects of a highly viscous lithosphere and a viscosity reduction in the D'' (Ammann *et al.* 2010; Nakada & Karato 2012). Supplied with the density model LSQ_5P, our inversion yields the viscosity profile $\mu_1$with a final misfit value of 0.23 (purple profile in Fig. 3-I). We note that an inversion with SSQ_5P results in a similar profile, but with a higher misfit value, and thus we have selected μ_1. μ_1 starts with 1.4×10^{20} Pa s in the asthenosphere, increasing by an order of magnitude in the lower upper mantle, then followed by $\approx 2 \times 10^{22}$ Pa s in the lower 2000 km. We also note that the inversion is solely optimized for geoid and mantle dynamics constraints, but matches the general GIA constraints of mantle viscosity.

Mantle viscosity profiles derived from geodetic observations tend to have poor sensitivity to lower mantle values. Lower mantle viscosity is primarily constrained by studies of variations in the degree two geoid ($\dot{J}_2$) induced by surface mass redistributions, that is glaciers and ice sheets. The $\dot{J}_2$ datum implies two permissible solutions for the lower mantle viscosity: $\approx 10^{22}$ and $(5-10) \times 10^{22}$ (Nakada *et al.* 2015). The higher value agrees with studies of sinking slabs speed (Butterworth *et al.* 2014), last Glacial Maximum sea levels (Nakada & Okuno 2016) and small perturbations to dynamic ellipticity (Pälike & Shackleton 2000; Morrow *et al.* 2012). This insight motivates us to consider a second viscosity profile, μ_2 (blue profile in Fig. 3-I), identical to μ_1 in the upper mantle, but stiffer by an order of magnitude in the deep mantle. It represents the higher end-member of permissible lower mantle viscosities. Together this yields a set of four viscosity profiles, shown in Fig. 3-I. Combinations of the four viscosity profiles (μ_1, μ_2, MF-2004 and SC-2006) and the two state estimates of present-day mantle heterogeneity (LSQ_5P and SSQ_5P) constitute the input parameters for eight RMs. Table 2 provides a summary of input parameters in the RMs.

Table 2. Overview of eight retrodiction models presented in this study.

Retrodiction model (RM)	Viscosity profile	Assumed present-day mantle state estimate	Maximum iteration
μ_1-SL	μ_1	LSQ_5P (SL2013sv+LLNL-G3D-JPS)	16
μ_1-SS	μ_1	SSQ_5P (SL2013sv+SEMUCB-WM1)	12
μ_2-SL	μ_2	LSQ_5P (SL2013sv+LLNL-G3D-JPS)	11
μ_2-SS	μ_2	SSQ_5P (SL2013sv+SEMUCB-WM1)	13
MF-SL	MF-2004	LSQ_5P (SL2013sv+LLNL-G3D-JPS)	14
MF-SS	MF-2004	SSQ_5P (SL2013sv+SEMUCB-WM1)	13
SC-SL	SC-2006	LSQ_5P (SL2013sv+LLNL-G3D-JPS)	15
SC-SS	SC-2006	SSQ_5P (SL2013sv+SEMUCB-WM1)	13

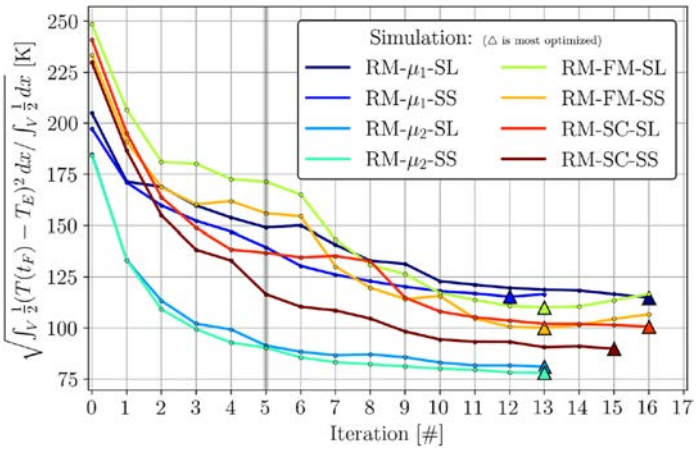

Figure 4. Difference between modelled and observed present-day temperature field as a function of iteration. The most minimized iteration is shown by a colour filled △ for each RM. For each RM we have performed a minimum number of 13 iterations. To mitigate the lack of a regularizing term in the misfit function, we analyse the results after five iterations. On average, the RMS of the difference is reduced by 55 per cent in all RMs. The highest reduction is achieved in SC–SS, with a reduction from 230 to 89 K.

2.3.1 Dynamic topography solutions

We compute dynamic topography from the well established propagator matrix technique (Richards & Hager 1984) in its compressible form (Panasyuk *et al.* 1996; Thoraval & Richards 1997). The semi-analytical solutions are commonly presented as kernels $K_l(r)$. The latter are interpreted as impulse-response functions that relate dynamic topography to a unit density anomaly of given wavelength (represented by spherical harmonic degree l) and radius r. Each spherical harmonic coefficient δh_{lm} for surface dynamic topography is computed in the spectral domain by

$$\delta h_{lm} = \int_{R_{\rm CMB}}^{R_{\rm Earth}} K_l(r)\, \delta\rho_{lm}(r)\, {\rm d}r. \tag{8}$$

In eq. (8), r is radius, $R_{\rm Earth}$ and $R_{\rm CMB}$ are the radii of the Earth at the surface and the CMB, respectively, and $\delta\rho_{lm}(r)$ is the density anomaly of SH degree l, and order m. Implicit in $K_l(r)$ is an assumption of effective mantle density $\Delta\overline{\rho}$ for the conversion of normal stress to topography (see Table 1). Note that the choice of $\Delta\overline{\rho}$ affects all wavelengths equally and thus cannot change the computed dynamic topography pattern. Fig. 3-II to 3-V visualizes the dynamic topography kernels for the four viscosity profiles μ_1, μ_2, MF-2004 and SC-2006 used in our study.

3 RESULTS

3.1 Iterative misfit functional minimization

Fig. 4 reports the RMS of the difference in the modelled and observed temperature at present-day for each iteration in our eight RMs. We performed a minimum of 13 iterations for each RM. The computational expense per iteration, per simulation totals 25 000 to 50 000 CPUh, depending on the model input parameters. On average, the RMS value is reduced by 55 per cent in all RMs. The highest reduction is achieved in SC-SS, where the initial RMS value of 230 K is reduced to 89 K. The lowest reduction occurs in μ_1-SS, where the initial RMS value of 197 K reduced to 116 K after 12 iterations.

Fig. 5 provides a spatial image of the iterative misfit reduction in μ_2-SL (left-hand panel, Figs 5-I to 5-VII) and μ_2-SS (right-hand panel, Figs 5-VIII to 5-XIV). In both panels, the top row visualizes the reference temperature fields, that is LS Q_5P (Fig. 5-I) and SSQ_5P (Fig. 5-VIII),

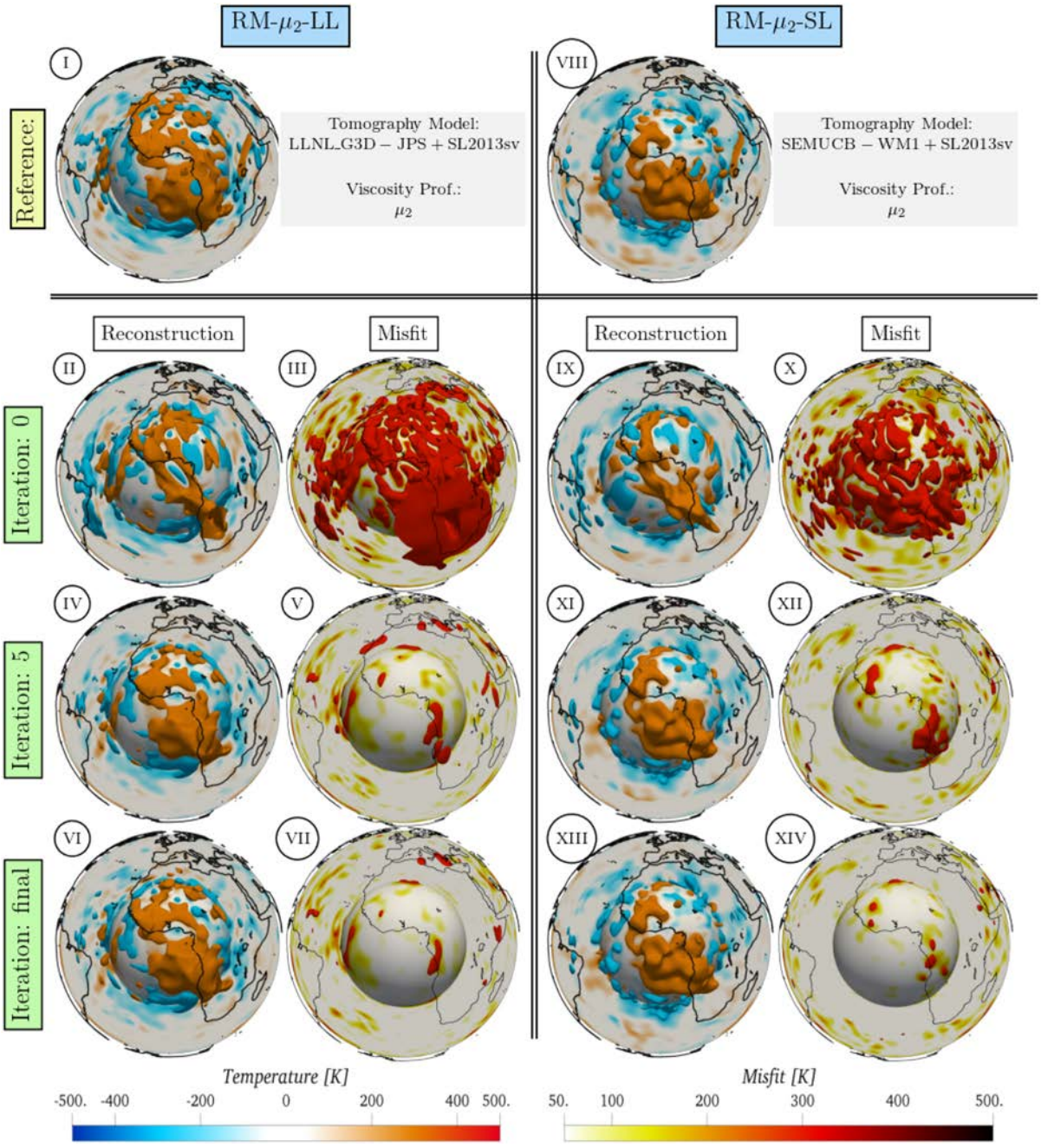

Figure 5. Misfit reduction for μ_2-SL (left-hand panel) and μ_2-SS (right-hand panel). In both panels the top row is the visualization of the reference temperature fields. (I) LSQ_5P obtained by combining SL2013sv (Schaeffer & Lebedev 2013) and LLNL-G3D-JPS (Simmons *et al.* 2015) and (VIII) SSQ_5P obtained by combining SL2013svand SEMUCB-WM1 (French & Romanowicz 2014). The reference temperature field (LSQ_5P for μ_2-SL and SSQ_5P for μ_2-SS) is used as initial guess for the initial condition at 50 Ma. II, IV, VI, IX, XI and XIII are the reconstructed temperature fields at present-day. III, V, VII, X, XII and XIV are the corresponding absolute differences between the modelled and observed temperature fields (error), after zeroth, fifth and final iteration (in both RMs 13). The error isosurface is chosen at 300 K. Taking μ_2-SL (left-hand panel) as an example: the model is initialized from LSQ_5P as the first guess for the unknown initial condition. The pattern after the first forward run differs substantially from the reference temperature field, in I. Successive model updates, shown after five adjoint iterations, improve the reconstructed final temperature field (see IV), and the general pattern of the African large low velocity province and the girdling subduction regions are restored, as confirmed by the much reduced error isosurface.

respectively, that represent the assumed present-day mantle state estimates. The latter are also taken as the first guess in all RMs for the unknown initial condition at 50 Ma. The second, third and fourth rows in each panel of Fig. 5 show the reconstructed final temperature field for the present day (Figs. 5-II, IV and VI for μ_2-SL, and Figs 5-IX, XI and XIII for μ_2-SS), and the corresponding absolute difference w.r.t. the assumed present-day mantle state estimate (error, Figs 5-III, V and VI for μ_2-SL and Figs 5-X, XII and XIIV), after the zeroth, fifth, and final (here 13th) iteration. Taking μ_2-SL (left-hand panel) as an example: the model is initialized from LSQ_5P as the first guess for the unknown initial condition. After the first forward run (iteration zero) from the necessarily incorrect first guess as the initial condition, the terminal state

shows narrow bands of hot material beneath the western margin of Africa extending to the southeastern parts of the continent (Fig. 5-II). The pattern differs substantially from the reference temperature field, LSQ_5P (Fig. 5-I), as expected, because the incorrect first guess for the initial condition yields an incorrect terminal state (see also Ghelichkhan & Bunge 2016). Large error amplitudes within the African hemisphere confirm this error. Successive model updates, shown after five adjoint iterations, improve the reconstructed final temperature field (Fig. 5-IV), and the general pattern of the African large low velocity province and the girdling subduction regions are restored, as confirmed by the much reduced error isosurface (Fig. 5-V). Misfit reductions in the subsequent iterations are minor and occur on shorter wavelengths, in agreement with the corresponding RMS curves (see Fig. 4), such that the error isosurface after 13 iterations (Fig. 5-VII) is significantly reduced.

3.2 Dynamic topography evolution

3.2.1 North America

We present our results by focusing upon four retrodiction models (μ_1-SL, μ_1-SS, μ_2-SL and μ_2-SS) that combine the two mantle state estimates with the two end-member viscosity profiles μ_1 and μ_2, involving a deep mantle viscosity of $\approx 2 \times 10^{22}$ and 10^{23} Pa s, respectively. For these models, Fig. 6 shows the retrodicted dynamic topography evolution with a view centred over North America. For all four RMs, we observe negative dynamic topography in the interior of North America in the early Cenozoic (at 50 Ma), which gives way to uplift, such that by about 30 Ma much of the negative dynamic topography has disappeared. The amplitude, location and uplift rates of dynamic topography vary, depending on the chosen model parameters (mantle heterogeneity input structure and viscosity profile), with the stiffer lower mantle viscosity profile μ_2 (see Fig. 3 I-red) yielding smaller amplitudes and slower uplift rates, as expected. For instance, at 40 Ma the North American interior and Central America see uplift rates exceeding 200 m Myr^{-1} in model μ_1-SL, while model μ_2-SL has an early Cenozoic uplift rate of about half that value. There is also early Cenozoic positive dynamic topography along the eastern margin of North America, giving way to subsidence. The trend is more pronounced in models μ_1-SL and μ_2-SL (Fig. 6 I,III), combining SL2013sv (Schaeffer & Lebedev 2013) and LLNL-G3D-JPS (Simmons *et al.* 2015), with dynamic subsidence rates at 35 Ma of about –100 m Myr^{-1}.

3.2.2 Australia

For the same four models, Fig. 7 shows the reconstructed dynamic topography evolution over Australia, the western Pacific and Antarctica. As seen before, there is a broadly similar evolution in all models. Dynamic topography is initially low over much of the Australian continent and centred towards the eastern and northern parts. In the early to mid-Cenozoic, between 50 and 40 Ma, eastern Australia uplifts, while subsidence occurs over the western and northwestern parts. At 30 Ma, uplift appears in the South and Southeast of Australia, as the continent travels over the high dynamic topography in the east. The late Neogene, at 10 Ma, sees subsidence in the northernmost part of the continent, in a trend that is more marked in models μ_1-SL and μ_2-SL (Fig. 7 I, III). The amplitudes and uplift rates of dynamic topography depend on the viscosity profile, as expected and noted before. But there is a more notable difference in the dynamic topography pattern between the two tomographic input structures. To this end, models μ_1-SS and μ_2-SS (Fig. 7 II, IV), combining SL2013sv (Schaeffer & Lebedev 2013) and SEMUCB-WM1 (French & Romanowicz 2014), yield a broad dynamic topography low in the early Cenozoic over much of Southeast Asia that gives way to regional uplift. Models μ_1-SL and μ_2-SL (Fig. 7 I, III) instead yield a broadly opposite trend. Starting from a dynamic topography high in the early Cenozoic over much of Southeast Asia, they give way to regional subsidence over the course of the Cenozoic.

3.2.3 Africa

Fig. 8 visualizes the reconstructed dynamic topography evolution over Africa since 50 Ma, again for μ_1-SL, μ_1-SS, μ_2-SL and μ_2-SS. In μ_1-SL (Fig. 8-I), Africa's dynamic topography is retrodicted to be high in the northwest for the early Cenozoic (at 50 Ma), giving way to broad subsidence in much of the northern part of the continent over the Cenozoic. Also the southern part of Africa is reconstructed with high dynamic topography for the early Cenozoic in a broad region from Madagascar into the South Atlantic. The extent of this domal region subsequently decreases as the peripheral portions subside and uplift focuses into two central regions: one in eastern South Africa, the other along the East African Rift system. Between 20 and 10 Ma, southeast Africa uplifts with 300 m Myr^{-1}, followed by an uplift of 50 m Myr^{-1} along the eastern edge. Model μ_1-SS shows a broadly similar dynamic topography evolution (Fig. 8-II). An initial high dynamic topography over Northwest Africa is followed by broad subsidence for much of northern Africa. In the southern parts of Africa, a broad region with initial high-standing topography focuses into two central regions, one in eastern South Africa, the other along the East African Rift system. The dynamic topography evolution differs substantially in models μ_2-SL and μ_2-SS with the stiffer lower mantle viscosity profile μ_2 (see Fig. 3 I-red) compared to the models using the μ_1 profile. Dynamic topography is generally low over much of Africa and the South Atlantic in the early Cenozoic (at 50 Ma Figs 8-III, IV), and a rapid dynamic topography increase with uplift rates of ≈100 m Myr^{-1} over Eastern and Southern Africa is delayed into the late Neogene.

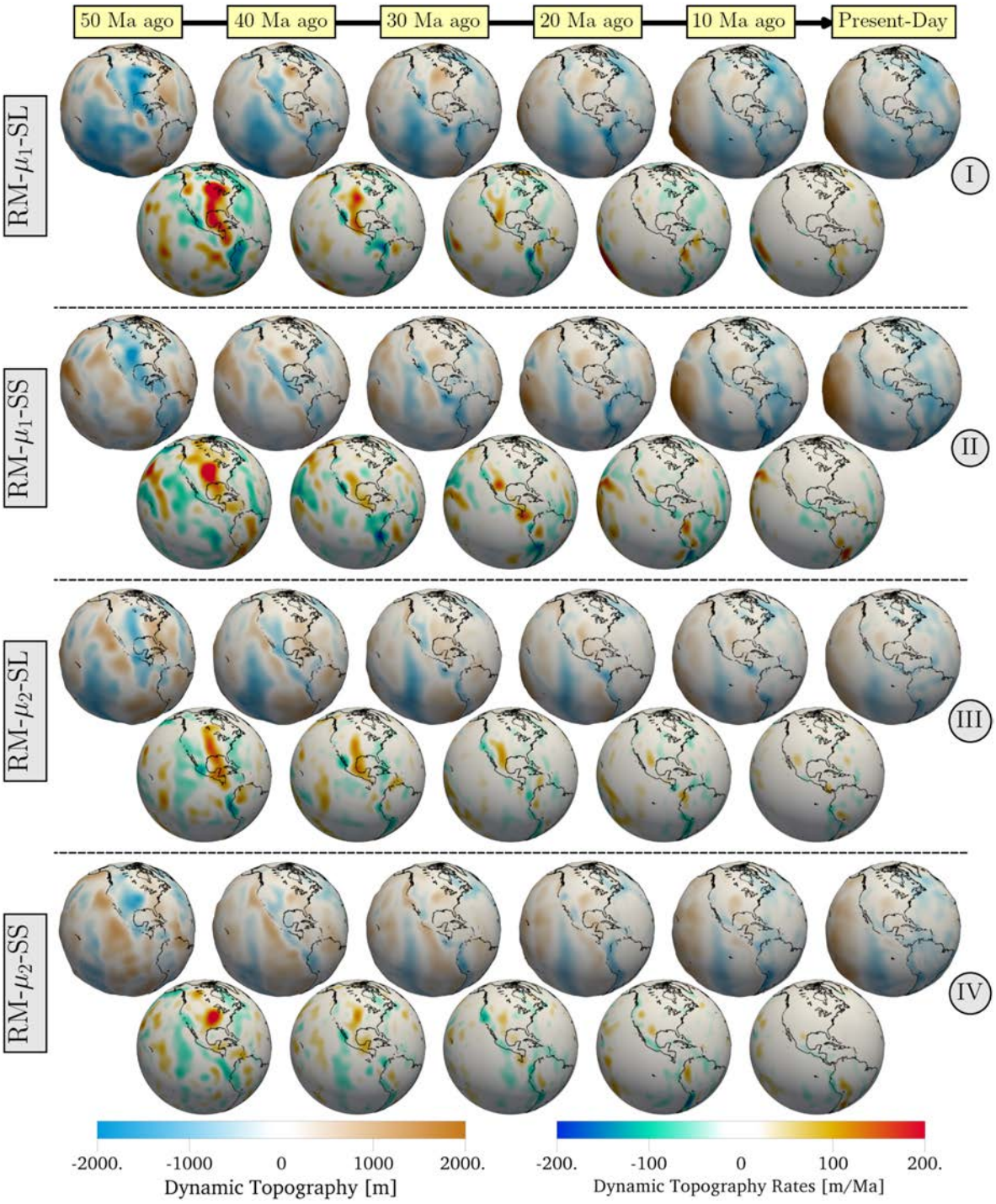

Figure 6. Retrodiction of dynamic topography (top-row) and its rates (bottom row) over North America in (I) μ_1-SL, (II) μ_1-SS, (III) μ_2-SL and (IV) μ_2-SS. The visualized coastlines are obtained by back-rotation of present-day coastlines using Young *et al.* (2019). Rates are calculated for time intervals of 10 Myr. In all four reconstruction models (RMs), negative dynamic topography in the interior of North America in the early Cenozoic (at 50 Ma) gives way to uplift, such that by about 30 Ma much of the continental-wide negative dynamic topography has disappeared. RMs with the stiffer lower mantle viscosity profile μ_2 (μ_2-SL and μ_2-SS) show smaller amplitude of dynamic topography and its uplift rates. For example, while μ_1-SL show uplift rates exceeding 200 m Myr^{-1} in the North American interior and Central America, μ_2-SL shows an early cenozoic uplift rate of about half that value. Pronounced in μ_1-SL and μ_2-SL, there is an early Cenozoic positive dynamic topography along the eastern margin giving way to subsidence at 35 Ma with –100 m Myr^{-1}.

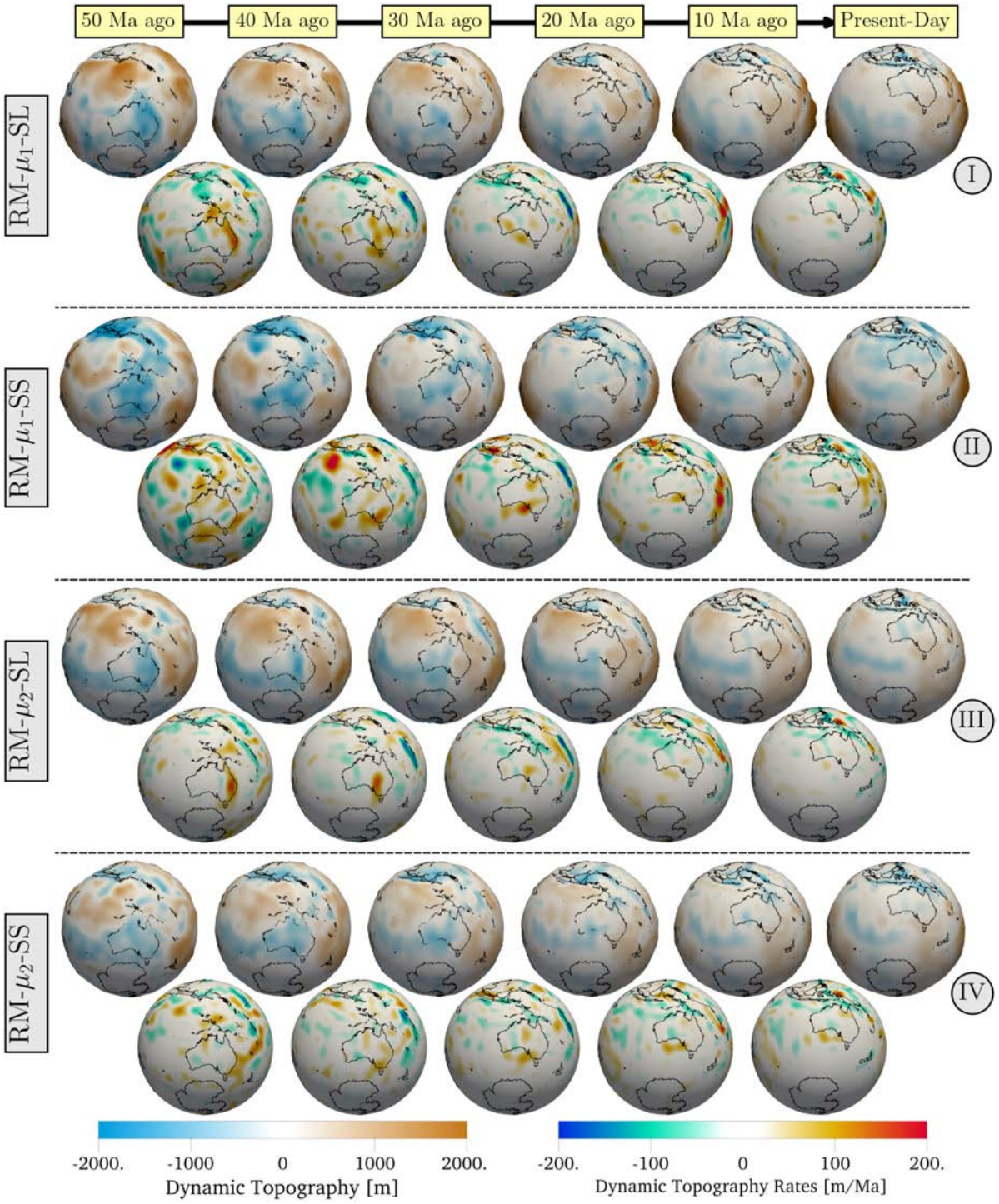

Figure 7. Same as Fig. 6 but over Australia and Antarctica. Dynamic topography is initially low over much of the Australian continent and centred towards the eastern and northern parts. Between 50 and 40 Ma, eastern Australia uplifts, while subsidence occurs over the western and northwestern parts. At 30 Ma, uplift moves to the south and southeast of Australia. At 10 Ma, the northernmost part of the continent subsides, in a trend that is more marked in models μ_1-SL and μ_2-SL. While μ_1-SS and μ_2-SS yield a broad dynamic topography low in the early Cenozoic over much of Southeast Asia that gives way to regional uplift, μ_1-SL and μ_2-SL instead yield a broadly opposite trend.

3.3 Deep mantle structure evolution

The development since 50 Ma of lateral temperature variations at ≈2500 km depth, that is 300 km above the CMB, together with arrows to visualize the horizontal mantle flow field is reported in Fig. 9. The retrodicted deep mantle evolution differs substantially in models μ_2-SL and μ_2-SS with the stiffer lower mantle viscosity profile μ_2 (see Fig. 3 I-blue) compared to models μ_1-SL and μ_1-SS using the weaker μ_1 (see Fig. 3 I-purple) profile. The latter show an accelerated evolution compared to the former. Looking first at μ_1-SL, we note that major up-

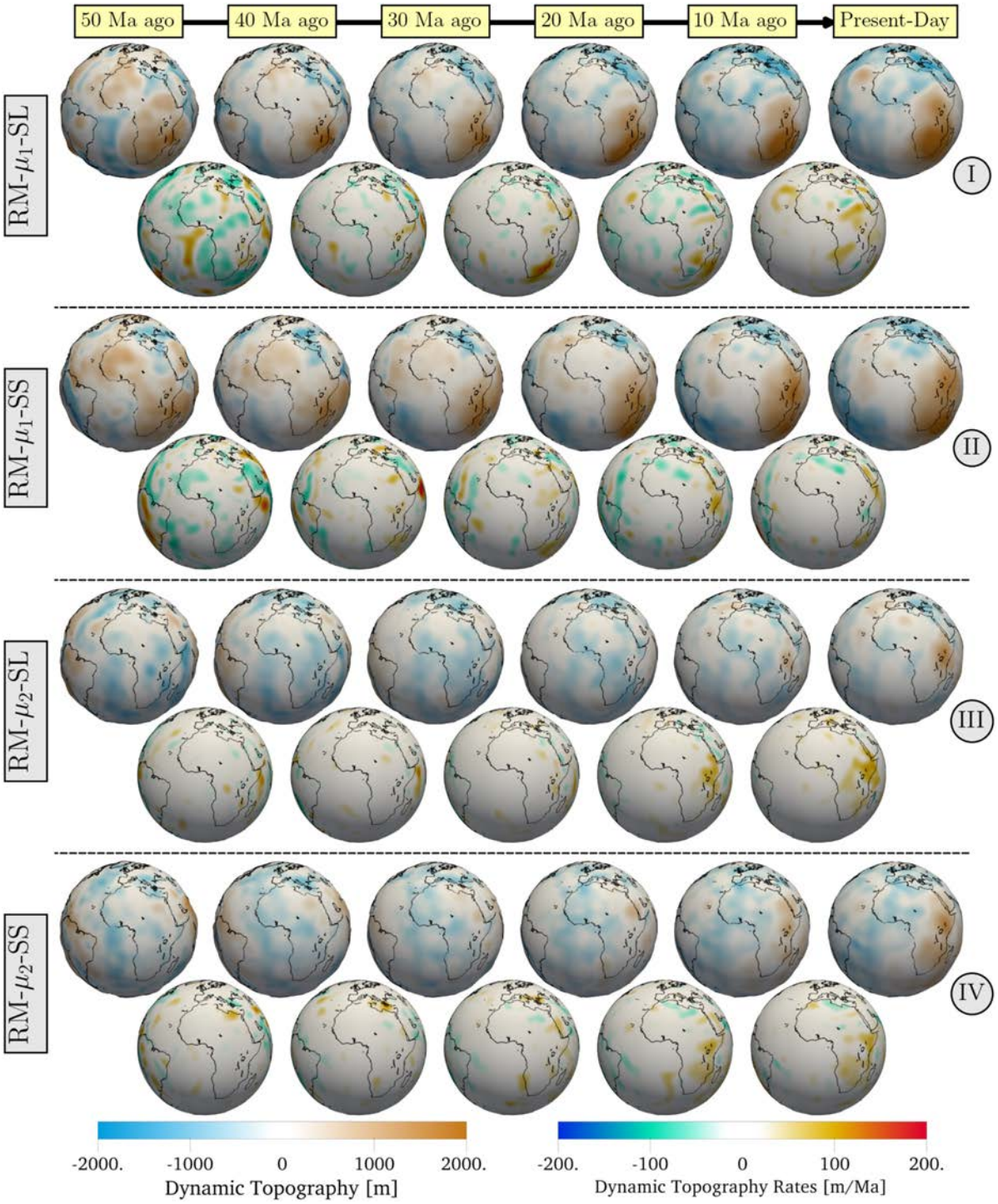

Figure 8. Same as Fig. 6 but over Africa. In μ_1-SL, Northwest of Africa is retrodicted high at 50 Ma, giving way to broad subsidence over the Cenozoic. The southern part of Africa is reconstructed with high dynamic topography since 50 Ma. The extent of this domal region subsequently transforms into two central regions: one in eastern South Africa, the other along the East African Rift system. Between 30 and 10 Ma, southeast Africa uplifts with rates exceeding 100 m Myr^{-1}, followed by an uplift of 50 m Myr^{-1} along the eastern edge. μ_1-SS shows broadly similar dynamic topography. In μ_2-SL and μ_2-SS with the stiffer lower mantle viscosity profile μ_2, dynamic topography is generally low over much of Africa and the South Atlantic since 50 Ma, with rapid uplift rates of ≈100 m Myr^{-1} over Eastern and Southern Africa at 10 Ma.

or downwelling regions display negligible lateral flow velocities, as expected. Examples include the cold regions beneath the Pacific Rim. Under North America, velocity vectors are directed eastward towards the Atlantic, while they point towards southern Africa beneath South America and Antarctica. Likewise, there is westward flow towards the Pacific below eastern Asia, at ≈3 cm yr^{-1}, while beneath western Asia the flow points northwest in the direction of the northern North Atlantic at ≈5 cm yr^{-1}. The average lateral flow velocity is ≈2.5 cm yr^{-1} . But higher flow velocities exist with a maximum of ≈7 cm yr^{-1} where material is supplied towards the upwelling LLSVP regions beneath Africa

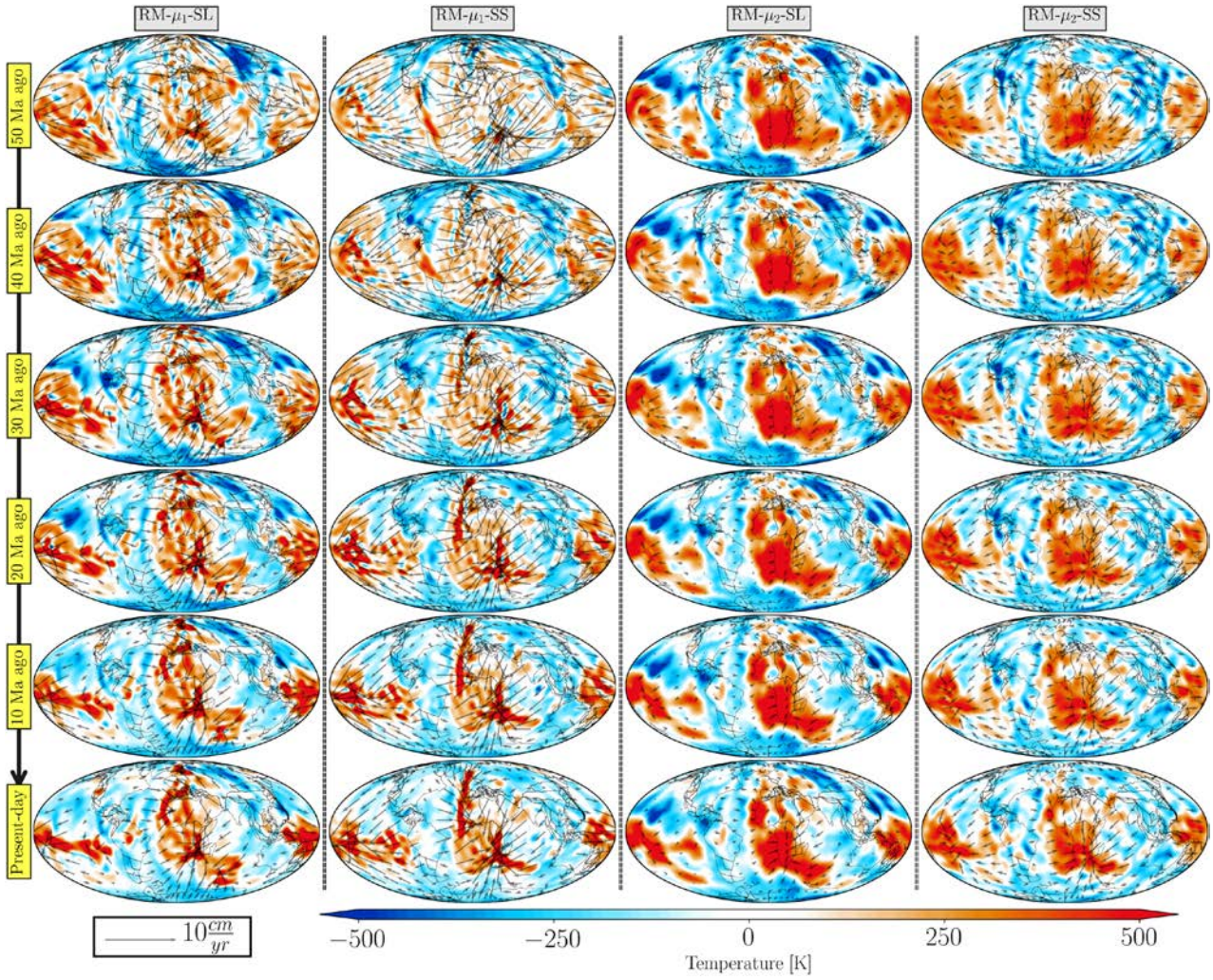

Figure 9. Evolution of CMB structure in four RMs, (I) μ_1-SL, (II) μ_1-SS, (III) μ_2-SL and (IV) μ_2-SS. Visualized is the deviatoric temperature (obtained by applying eq. (2) on the temperature field and subtracting the average temperature profile from absolute temperature), and lateral velocity ($\boldsymbol{u} - (\boldsymbol{u}.\boldsymbol{e_r})\boldsymbol{e_r}$) fields at 300 km above the CMB. Major down or upwellings show negligible lateral velocities beneath western Americas, and northwest Pacific. The retrodicted deep mantle evolution differs substantially in models with the stiffer lower mantle viscosity profile μ_2 (see Fig. 3-I-red) compared to models with the weaker μ_1 (see Fig. 3-I-purple) profile. The latter show an accelerated evolution compared to the former.

and the central Pacific. The fast flow velocities result in substantial temporal change of the temperature field. Specifically, the convergence of flow towards upwelling regions shapes the hot anomalies into narrow hot bands of plumes, both in the African and the Pacific hemisphere. A broadly similar behaviour occurs in μ_1-SS (Fig. 9-II). Retrodicted thermal structure and lateral flow velocities for the two RMs using the μ_2 viscosity profile are shown in Figs 9-III/IV. The velocity pattern is similar in μ_2-SL and μ_2-SS relative to μ_1-SL and μ_1-SS. But the average lateral flow velocities are considerably lower ($\approx$0.8 cm yr^{-1} in μ_2-SL and $\approx$ 1.2 cm yr^{-1} in μ_2-SL), with a maximum speed of 2.3 cm yr^{-1} for μ_2-SL and 2.9 cm yr^{-1} in μ_2-SL. Consequently, there is reduced temporal change in the thermal fields. The general pattern of the deep mantle structure thus seems to be more stationary.

3.4 Material transport measured by flow trajectories

The history of mantle velocity fields computed by geodynamic flow retrodictions allows one to compute previous positions of mantle material for any sampling location of our choice. As an example, we turn to the uppermost mantle beneath Europe in Fig. 10, because some Cenozoic volcanic centres in this region have been linked to putative upwelling mantle plumes, for instance, beneath the Eifel region (Ritter *et al.* 2001). We compute the flow trajectories through 3-D tracking of particles. The particles are evenly distributed at present-day with $\approx$100 km spacing at 120 km depth at the top of the low viscosity asthenosphere (Fig. 3 I). Tracking is then performed as a post-processing step in our simulations by backward-in-time integration along the reconstructed 3-D mantle velocity field. To simplify the visualization, we present the particle position at earlier times by projections onto the surface. Fig. 10 shows results for μ_1-SL, μ_1-SS, μ_2-SL and μ_2-SS for a subset of the trajectories. The trajectories vary regionally in length and direction owing to complex flow velocity fields. For example, in μ_1-SL the extent of lateral movements in western Europe is broadly from the North Atlantic, while in southwestern Europe it is broadly from the Central

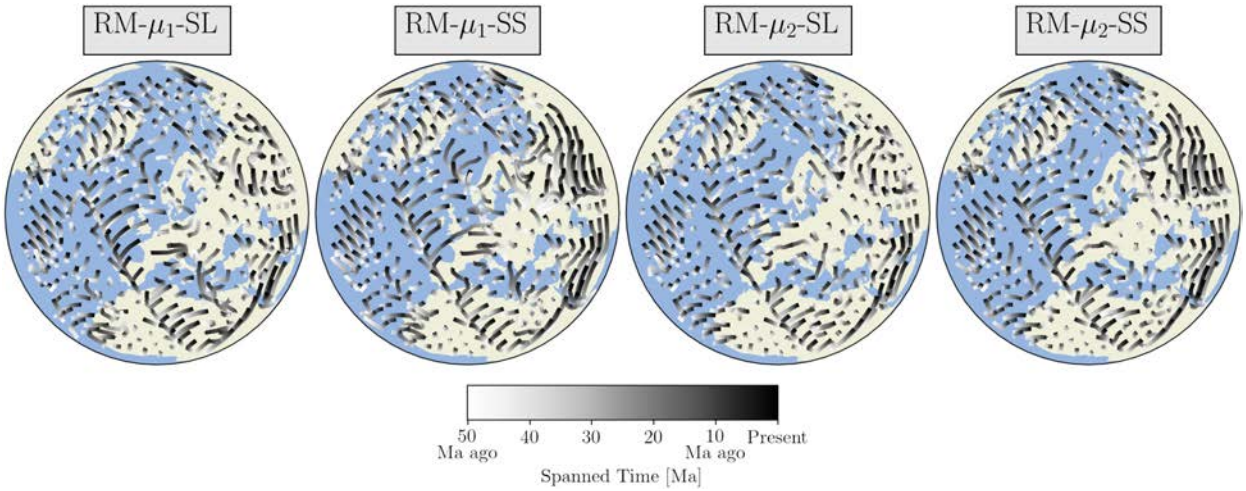

Figure 10. Lateral component of asthenospheric streamlines in four RMs of μ_1-SL, μ_1-SS, μ_2-SL and μ_2-SS. Tracking is performed by backward-in-time integration of the reconstructed velocities (i.e. only as post-processing) for equally distributed particles that are located at 120 km depth. The lateral components are then computed by projections of the 3-D streamlines onto a unit sphere. The trajectories vary regionally in length and direction owing to complex flow velocity fields. Broadly speaking, the retrodiction models show that material underneath Europe has been fluxed in from either northwestern or southwestern locations during the past 50 Myr.

Atlantic. In other words, material currently located in μ_1-SL at 120 km depth in these two regions has been fluxed in from either northwestern or southwestern locations during the past 50 Myr. The patterns in μ_1-SS, μ_2-SL and μ_2-SS are in general agreement with μ_1-SL.

3.5 Upper mantle flow, sublithospheric stresses, Farallon-slab and Afar-plume evolution in μ_2-SL

3.5.1 Upper mantle flow

μ_2-SL combines the mantle heterogeneity model LSQ_5P with the viscosity profile μ_2. Having a modest time evolution (see Fig. 9 column III) compared to models using the μ_1 profile, it lends itself as a conservative end-member for temporal changes in our retrodiction models. Thus, we report from here on estimates for upper mantle flow, sublithosphere stresses, the Farallon slab and Afar plume evolution only for μ_2-SL. Fig. 11 visualizes the horizontal upper mantle flow field in nine equidistant layers from 90 to 700 km depth since 50 Ma. We also show the lateral temperature variation at 700 km depth. The top row reports the flow field for the North Atlantic region with a view centred over western Europe. In general the upper mantle beneath the North Atlantic shows westward flow at ≈ 5 cm yr^{-1} . Beneath the northern part of western Europe, the flow field is directed to the southeast. In other words, there is an influx from the northwest into the upper mantle of northwestern Europe albeit with temporal variations in amplitude and direction. The upper mantle beneath the Iberian peninsular and parts of France instead experiences influx ($\approx$1 cm yr^{-1}) from the southwest, with an approximate source region located offshore of northwest Africa. The bottom row of Fig. 11 visualizes upper mantle flow in the Central Pacific, with a view centred near the current location of Hawaii. Also in this region there is considerable temporal and spatial variability of the upper mantle flow field. In particular, there are broad regions where the upper mantle flow field is directed at an angle to the overlying Pacific Plate motion (shown by transparent vectors at the surface). Overall, since 50 Ma, there is eastward flow in the East Pacific, westward flow in the West Pacific and radial spreading in the central Pacific. The latter occurs in response to influxing hot anomalies from the deeper mantle into the upper mantle, driven by deep-mantle thermal anomalies, and clearly visible at 30 Ma.

3.5.2 Sublithospheric stress fields

Fig. 12 reports the evolution of the sublithospheric tangential stress field imparted by viscous flow at a depth of 180 km in our conservative end-member model μ_2-SL. We calculate tangential stresses as the magnitude of the tangential component of the surface traction, which itself is calculated by computing the inner product of the stress tensor and the surface normal (that is the radial) vector. The stress field varies in space and time, as expected for time dependent mantle flow, with values in the range of $\approx 10^5 - 10^6$ Pa. For the Australian region (Fig. 12-I), stress magnitudes are initially small beneath the continent, with larger amplitudes (5×10^6 Pa) developing as the continent moves away from Antartica. The fast moving Indian plate at 50 Ma is also associated with tangential stresses in the range of $\approx 10^6$ Pa, with amplitudes decreasing at later times. Beneath North America (Fig. 12-II) tangential stresses achieve values of $\approx 5 \times 10^5$ Pa, while higher values of $\approx 5 \times 10^6$ Pa are reached beneath the oceanic plates to the west. In comparison, stress levels remain smaller in the African hemisphere (Fig. 12-III), presumably because of slower plate velocities there. Importantly, the stress field displays a spatial coherence over distances of $\approx$ 1000-5000 km.

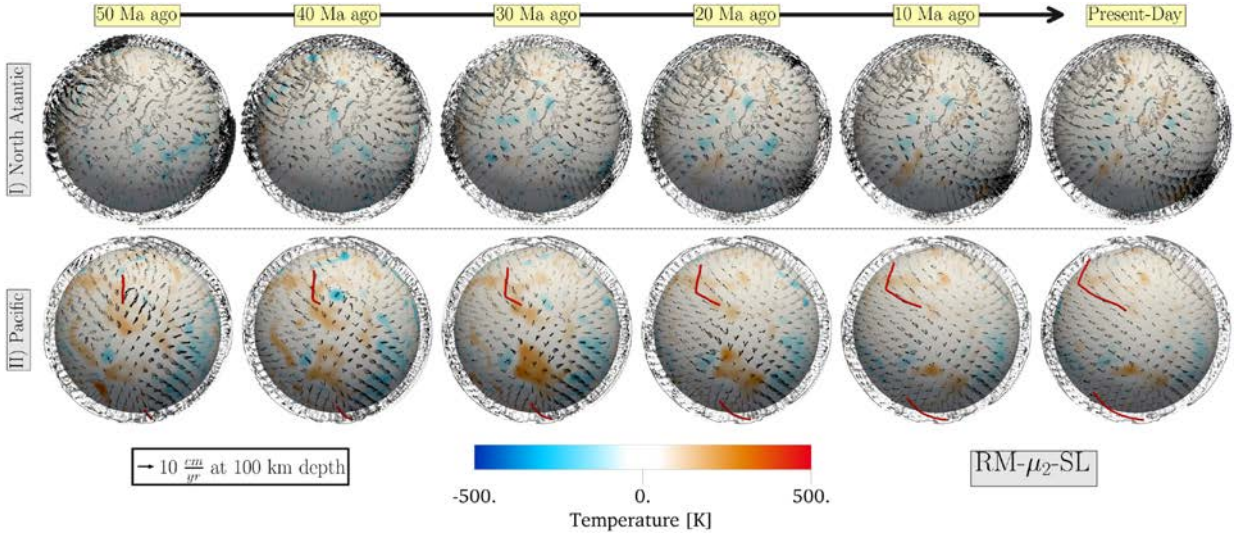

Figure 11. Evolution of asthenospheric lateral velocities ($\boldsymbol{u} - (\boldsymbol{u}.\boldsymbol{e_r})\boldsymbol{e_r}$) and deviatoric temperatures (obtained by applying eq. (2) on the temperature field and subtracting the average temperature profile from absolute temperature) in μ_2-SL in (I) North Atlantic and (II) Pacific. Visualized are deviatoric temperature fields at 700 km deep, and lateral velocities shown on nine equidistant layers above. The velocity vectors at the surface are visualized in transparency mode. The red curves in II are reconstructions of the Hawaiian (upper curve) and Louisville (lower curve) hotspot tracks using Young *et al.* (2019). The upper mantle beneath the North Atlantic shows westward flow with ≈5 cm yr^{-1}. Beneath the northern part of western Europe the flow field is directed to the southeast. The upper mantle beneath the Iberian peninsular and parts of France instead experiences influx from the southwest, with an approximate source region located offshore of northwest Africa. In II, there is eastward flow in the East Pacific, westward flow in the West Pacific and radial spreading in the central Pacific. The latter occurs in response to influxing hot anomalies from the deeper mantle into the upper mantle, driven by deep-mantle thermal anomalies, and clearly visible at 30 Ma.

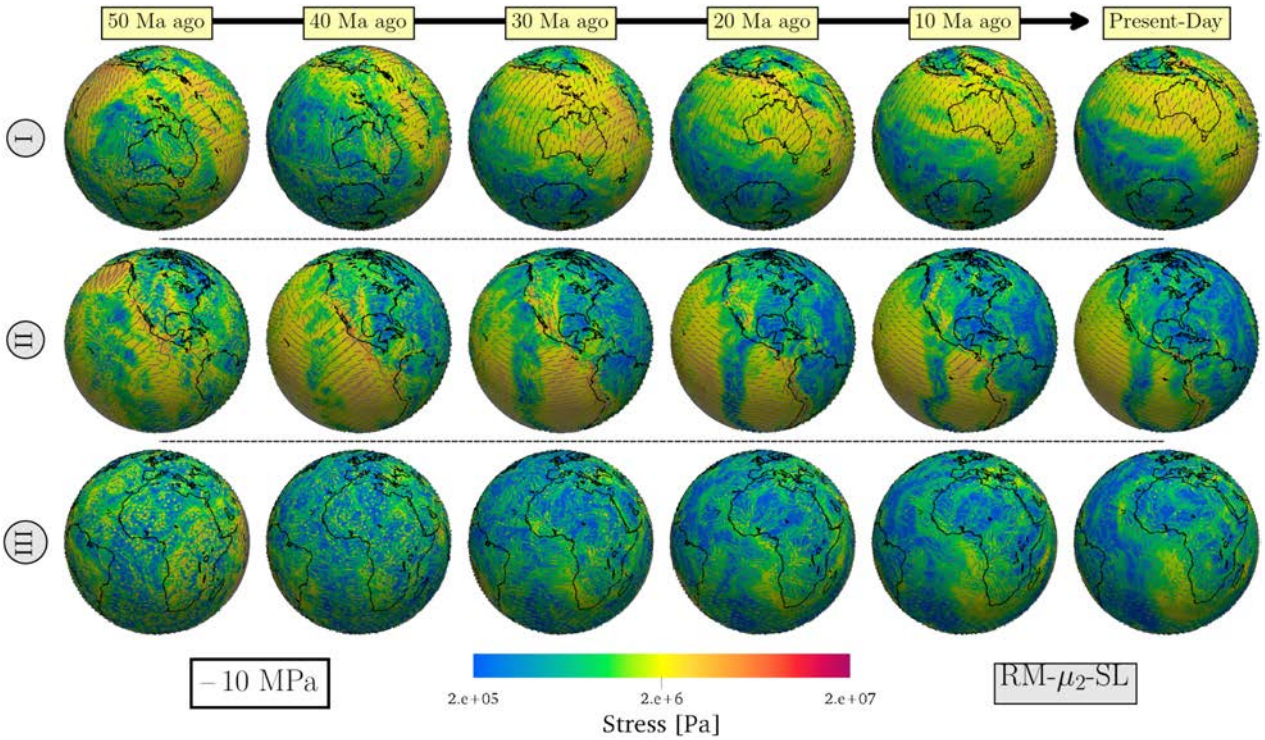

Figure 12. Evolution of the tangential stresses imparted by viscous flow at a depth of 180 km over (I) Australia, (II) North America and Pacific and (III) Africa. Tangential stress field is calculated as the magnitude of the tangential component of surface traction, which itself is calculated by computing the inner product of the stress tensor and surface normal vector The stress field varies in space and time, as expected for time dependent mantle flow, with values in the range of $\approx 10^5 - 10^6$ Pa. Importantly, the stress field displays a spatial coherence over distances of $\approx 1 - 5 \times 10^3$ km.

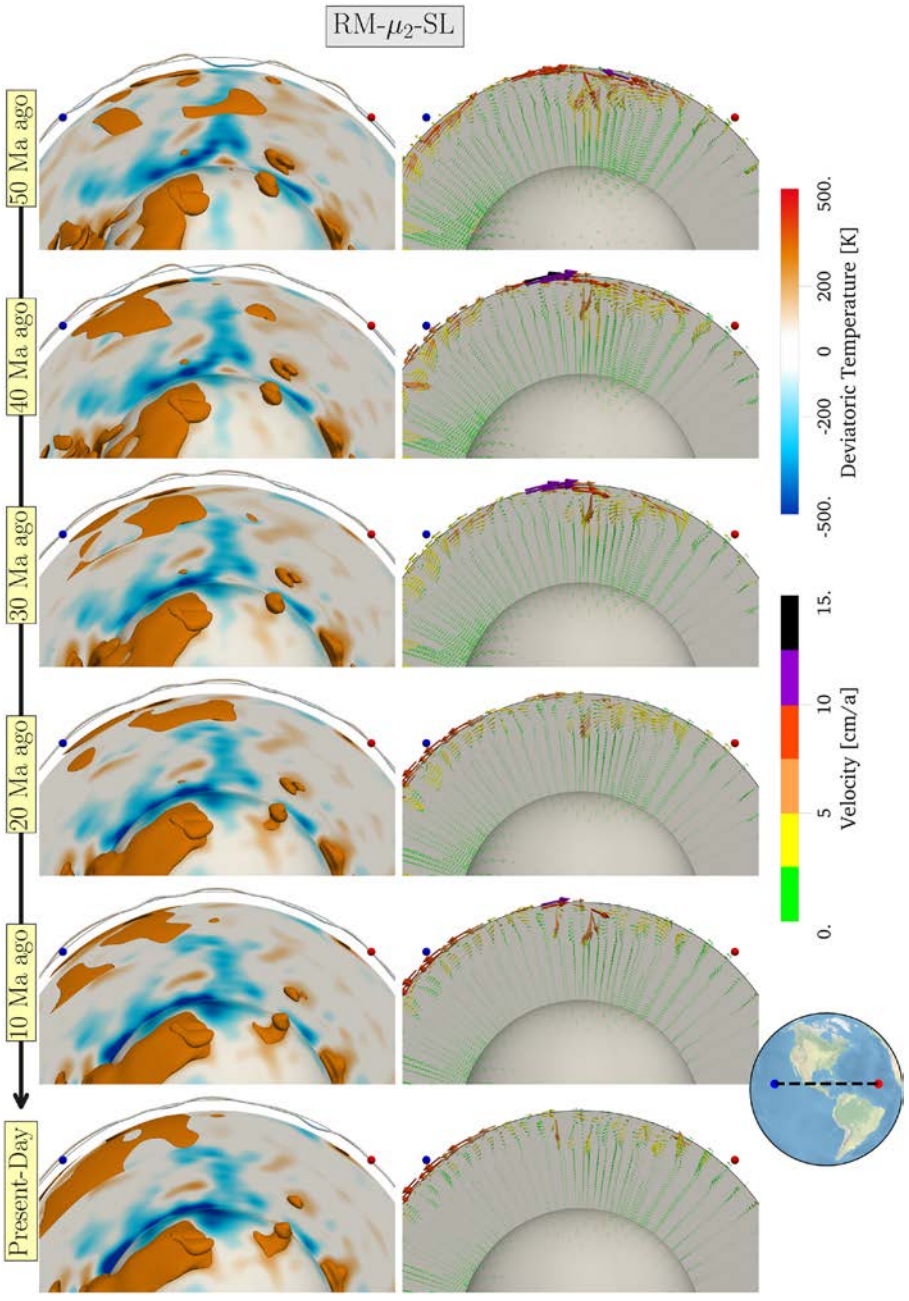

Figure 13. This figure should be rotated counter clock-wise as in the original manuscript. As for all the other figures, please remove the frame.Evolution of mantle temperature and dynamic topography (left-hand panel), and velocity field (right-hand panel) beneath North America in μ_2-SL (SL2013sv and LLNL-G3D-JPS with μ_2 profile). The visualizations are obtained by a cross-section of the computational domain around the great circle passing through red (40W, 15N) and blue (130W, 15N) points, and a spherical cross-section at the CMB. Point of view is chosen to be from south, focused on mid-mantle. Deviatoric temperature is obtained by using eq. (2) and subtracting the average temperature profile from absolute temperature. The isosurface is chosen at $+300$ K. Velocity vectors are visualized on the vertical cross section and within 100 km of the CMB. The Farallon slab is restored at shallow depths and sinks synchronous to the westward movement of the Americas. The subsequent uplift at 40 Ma in North America is then accompanied by westward flowing asthenosphere material.

3.5.3 Regional mantle flow evolution: examples of Farallon-slab and Afar-plume motion

In Section 3.2.3, we presented dynamic topography retrodictions over North America and Africa. Here we link them to the underlying mantle convection currents for model μ_2-SL. To this end, Figs 13 and 14 report in their left-hand columns the thermal evolution beneath North America (Fig. 13) and Afar (Fig. 14). A vertical cross section displays the deviatoric temperature field (thermal anomalies w.r.t. the radial profile). Shown is also a 3-D isosurface ($+300$ K) to outline regions of elevated temperature. The right-hand columns show flow velocity vectors. Furthermore, we visualize the dynamic topography along the great circle of the cross sections, to link to the flow induced topography

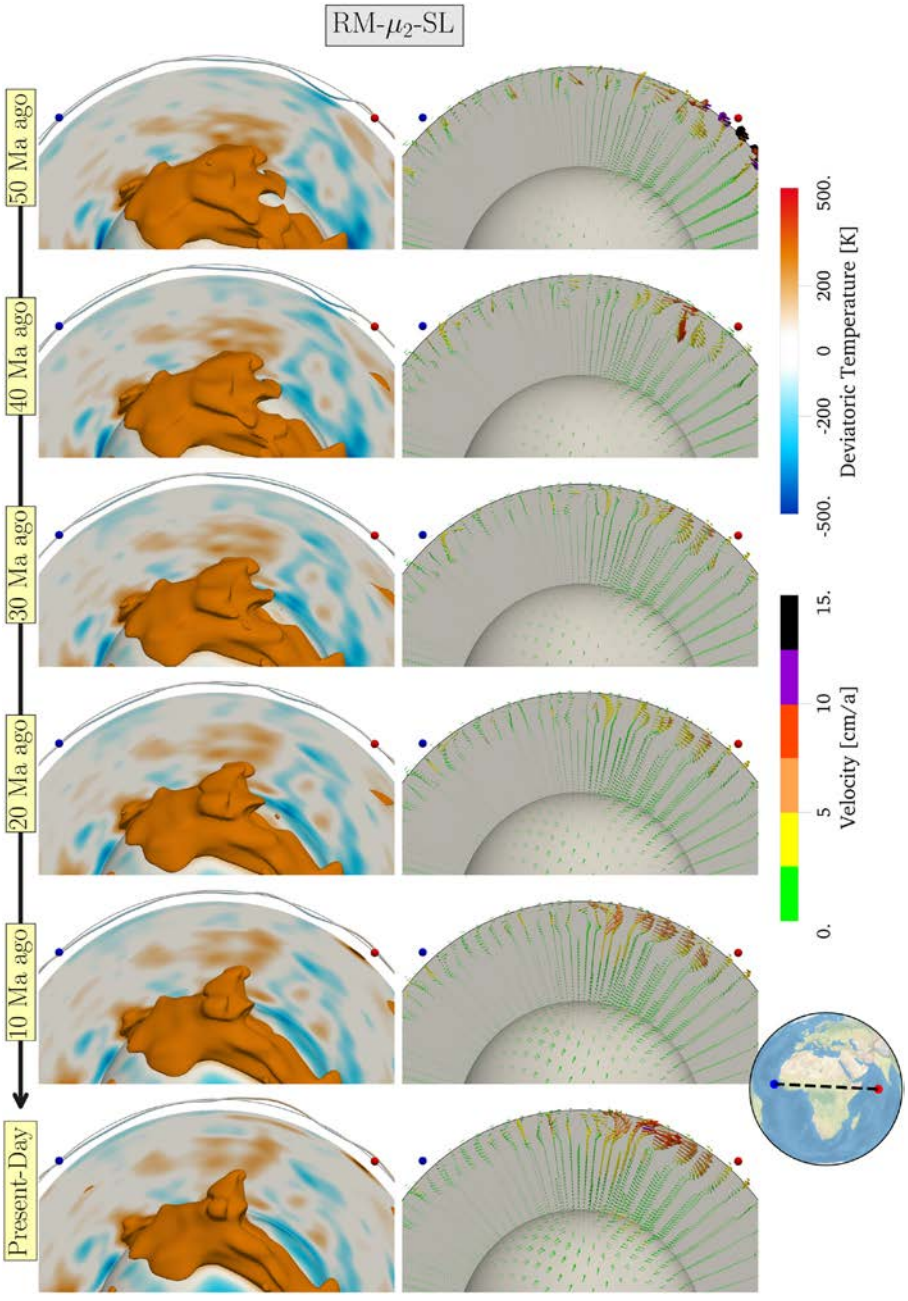

Figure 14. Evolution of mantle temperature and dynamic topography (left-hand panel), and velocity field (right-hand panel) for Afar in μ_2-SL (SL2013sv and LLNL-G3D-JPS with μ_2 profile). Details are the same as Fig. 13. The cross section is along a great circle that passes through red (65E, 5N) and blue (25W, 9N) points. The Afar plume beneath East Africa is initially located at mid-mantle depths at 50 Ma, rising to the surface with an eastward tilt at 15 Ma. Consequently, the reconstructed dynamic topography is initially low, with significant flow induced uplift along the East African Rift starting from 15 Ma. Strong eastward lateral motion (up to 6 cm yr^{-1}) is induced by the arrival of hot anomalies in the asthenosphere.

by the convective currents. Fig. 13 identifies the Farallon slab as the origin for the low dynamic topography of North America at 50 Ma. The slab is restored at shallow depths and sinks synchronous to the westward movement of the Americas. The subsequent uplift at 40 Ma in North America is then accompanied by westward flowing asthenosphere material.

Fig. 14(left-hand panel) reveals a history of mantle upwelling beneath Africa. The Afar plume beneath East Africa is initially located at mid-mantle depths at 50 Ma, rising to the surface with an eastward tilt at 15 Ma. Consequently, the reconstructed dynamic topography is initially low, with significant flow induced uplift along the East African Rift starting from 15 Ma. Furthermore, Fig. 14(right-hand panel) illustrates that strong eastward lateral motion (up to 6 cm yr^{-1}) is induced by the arrival of hot anomalies in the asthenosphere.

4 DISCUSSION

We have explored high-resolution global mantle flow retrodictions. To this end, we have built upon our previous work presented by Colli *et al.* (2018) and investigated key input parameters for restoring past mantle evolution. We applied the compressible adjoint equations (Ghelichkhan & Bunge 2016) to generate a suite of geodynamically plausible mantle flow models with ≈670 million finite element nodes. While the high numerical resolution provides the means to represent mantle flow at Earth-like convective vigor, it poses a computational challenge: one iteration of a retrodiction model requires on average 40 000 CPUh, translating to a total of ≈4 million CPUh for computing 13 adjoint-forward iterations of the eight models in this study. The high computational cost necessarily limits the ability to perform broader parameter surveys.

The key input information for the retrodictions comes from two estimates of the present-day mantle heterogeneity state, together with four geodynamically motivated radial viscosity profiles. The state estimates are obtained from two whole-mantle tomography models: LLNL-G3D-JPS (Simmons *et al.* 2015), which uses ray tracing algorithms for joint inversions of shear and compressional waves that account for internal undulations and multipathing of crustal, regional and triplicated seismic phases with ≈100 million traveltimes; and SEMUCB-WM1 (French & Romanowicz 2014) with a semi-waveform inversion approach, in which misfit derivatives are approximated using non-linear asymptotic coupling theory. For depths shallower than 400 km, we supplemented these models with SL2013sv (Schaeffer & Lebedev 2013), motivated by the high upper mantle resolution in this model. We selected these studies because they are robust inversions of seismic shear speeds that capture major mantle structures. These models have also been used in previous tectonic and geodynamic interpretations of seismic structure (e.g. French & Romanowicz 2015; Simmons *et al.* 2015; Richards *et al.* 2020b, a; Hoggard *et al.* 2020). Nonetheless, we must be clear that significant further advances exist in the seismic illumination of the mantle state, including innovative approaches for traveltime and waveform modelling approximations (e.g. Houser *et al.* 2008; Debayle *et al.* 2016), incorporation of finite frequency and full waveform inversion theories (e.g. Montelli *et al.* 2006; Fichtner *et al.* 2009; Tape *et al.* 2009; Obayashi *et al.* 2013; Bozdağ *et al.* 2016; Lei *et al.* 2020; van Herwaarden *et al.* 2020), added seismic phases and normal modes (e.g. Koelemeijer *et al.* 2016; Durand *et al.* 2017), efforts to image the D" structure (Tkalčić *et al.* 2002), as well as joint constraints from seismic-geodynamic observations (e.g. Simmons *et al.* 2010; Lu *et al.* 2019). These studies provide viable alternatives to represent the mantle heterogeneity state. Augmented with efforts to improve seismic model regularizations with objective regularizing and averaging techniques (e.g. Zaroli *et al.* 2013; Zaroli 2016), and the emergence of collaborative seismic models (Fichtner *et al.* 2018), this bodes well for the use of seismic studies in mantle flow retrodictions.

We must also be clear that the geodynamic analysis of seismic mantle state estimates remains under debate, permitting interpretations of deep mantle structure primarily by elevated temperature (Schuberth *et al.* 2009a, b, 2012; Simmons *et al.* 2009; Davies *et al.* 2012, 2015), or combinations of thermal and compositional effects (Lu *et al.* 2020; McNamara 2019). For the sake of simplicity, we opted for a purely thermal interpretation of the seismic heterogeneity structure, which we mapped to temperature and density using a self-consistent model for a pyrolitic mantle that includes the effects of anelasticity. Our choice is supported by recent seismic studies that provide a more detailed image of deep mantle heterogeneities (Hosseini *et al.* 2020) together with new seismic-geodynamic interpretations that seek to deflate the large-scale deep mantle low-velocity zones (Davaille & Romanowicz 2020). Further support for predominantly thermal interpretations of large-scale deep mantle anomalies comes from recent geochemical investigations of kimberlitic rocks (Tappe *et al.* 2020) showing that kimberlites from above the African LLSVP lack anomalous tungsten signatures, as well as from seismic attenuation analyses in the lowermost mantle (Liu & Grand 2018). Nevertheless, the interpretation of large-scale deep mantle heterogeneity as combinations of thermal and compositional effects remains viable, with a number of geochemical arguments for the existence of preserved deep mantle reservoirs (Zindler & Hart 1986; Lyubetskaya & Korenaga 2007; Davies 2009), for which the use of thermochemical adjoint inversions (Ghelichkhan & Bunge 2018) is indicated.

We chose four viscosity profiles that account for a highly viscous lithosphere, a weak asthenosphere, followed by a broad increase into the lower mantle, and a subsequent viscosity reduction in the lowermost mantle. These profiles include two previously published studies: MF-2004 (Mitrovica & Forte 2004), optimized for mantle and ice age dynamics, and SC-2006 (Steinberger & Calderwood 2006), obtained by fitting mineralogical parameters to geoid constraints. In addition, we derived two profiles, inverted for geoid and CMB topography constraints, that are consistent with the chosen mantle heterogeneity structure. The profiles bracket a range of admissible lower mantle viscosity values from 1.7×10^{22} to 10^{23} Pa s, and agree with studies of Chandler wobble and tidal deformation (Nakada *et al.* 2015), as well as recent mineral physics modelling (Reali *et al.* 2019). We note that the upper bound agrees with studies of sinking slab speeds (Butterworth *et al.* 2014), last glacial maximum sea levels (Nakada & Okuno 2016) and small perturbations of dynamic ellipticity from the analysis of magnetic susceptibility records (Pälike & Shackleton 2000). The lower bound is supported by the higher perturbation in dynamic ellipticity deduced from sedimentary cores [Lourens *et al.* (2001); see Morrow *et al.* (2012) for a review]. We eased the presentation by focusing on the two end-member viscosity profiles (μ_1 and μ_2). However, the dynamic topography evolution in retrodiction models using the more sophisticated viscosity profiles (i.e. MF-2004 and SC-2006) is broadly similar to the results reported here (see Figs 15 and 16 for North American and African examples), with agreement closer to the stiffer μ_2 profile, as expected from the dynamic topography kernels (Fig. 3).

The retrodictions are sensitive in their computed dynamic topography evolution to the assumed present-day mantle state and rheology. This observation motivates us to compare the retrodicted dynamic topographies with inferences on epeirogenic motion gleaned from the geological record to asses the underlying input information in our retrodiction models. One constraint on dynamic topography lows come from palaeoshoreline maps (e.g. Smith *et al.* 1994), whereas interregional hiatus surface can serve as a proxy for dynamic topography highs (e.g. Friedrich *et al.* 2018; Hayek *et al.* 2020). However, we emphasize that there exist many other dynamic topography indicators, as reviewed recently by Hoggard *et al.* (2021).

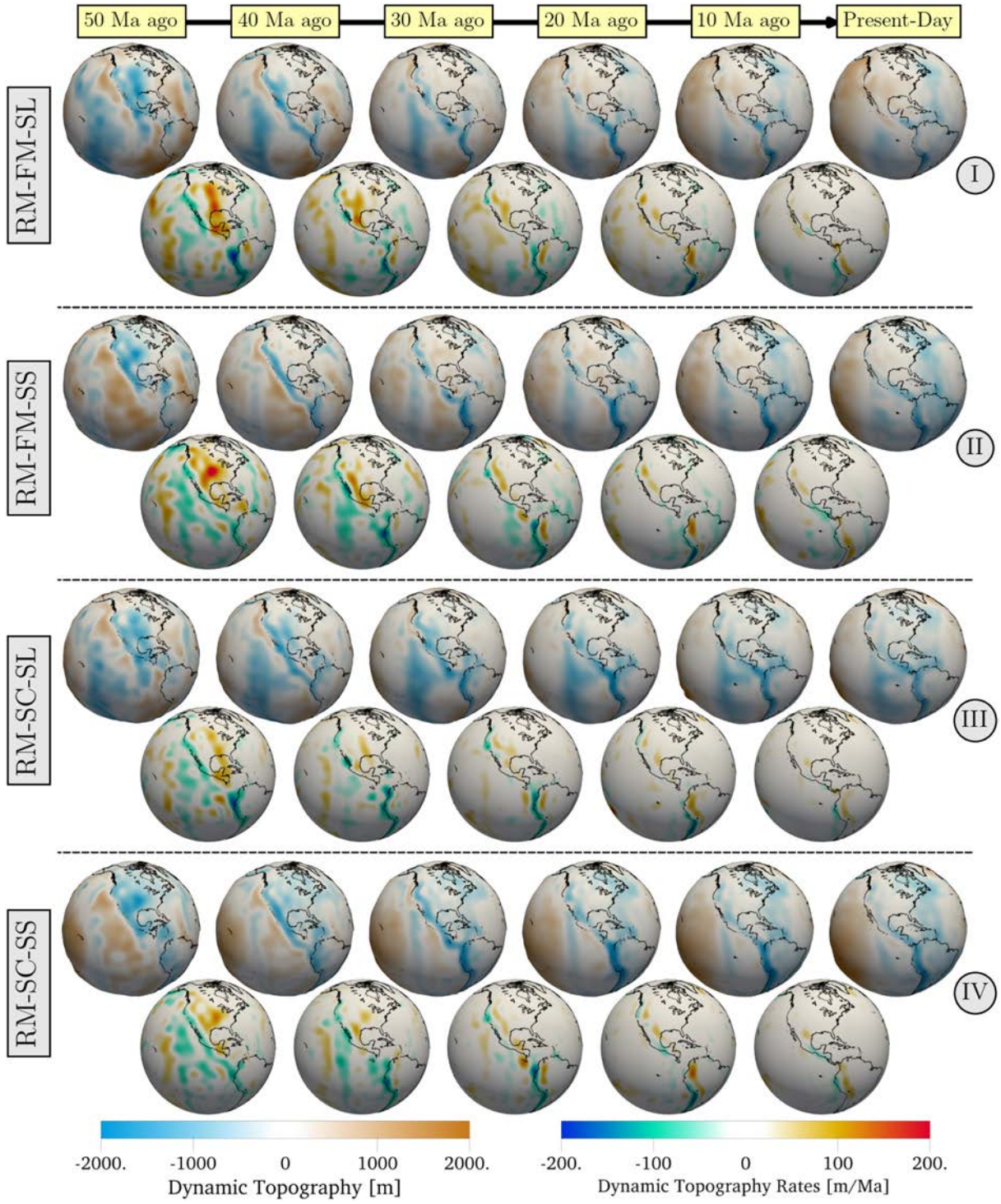

Figure 15. As in Fig. 6, but for in (I) MF-SL (SL2013sv and LLNL-G3D-JPS with MF-2004 profile), (II) MF-SS (SL2013sv and SEMUCB-WM1 with MF-2004 profile), (III) SC-SL (SL2013sv and LLNL-G3D-JPS with SC-2006 profile) and (IV) SC-SS (SL2013sv and SEMUCB-WM1 with SC-2006 profile). The dynamic topography evolution in retrodiction models using the more sophisticated viscosity profiles (i.e. MF-2004 and SC-2006) is broadly in agreement with the stiffer μ_2 profile. Negative dynamic topography in the interior of North America at 50 Ma disappears by about 30 Ma. The rates of uplift in MF-SL and MF-SS exceed the rates in the other two models. Arriving at present-day, the eastern margin of North America undergoes subsidence in all four models.

Looking at North America first, we find that our end-member retrodiction models (μ_1-SL, μ_1-SS, μ_2-SL and μ_2-SS) all produce a dynamic topography low for the earliest retrodicted time, that is the early Eocene, over the interior of the continent, regardless of the tomographic input structure. The low has largely disappeared by mid-Eocene, which is somewhat later than its late Cretaceous-Palaeocene demise inferred by palaeoshorelines. The occurrence of a Cretaceous mid-continental depression has long been linked to the descent of the subducting Farallon plate in the mantle (e.g. Bond 1976; Mitrovica *et al.* 1989; Burgess *et al.* 1997), which is also seen in our models (see

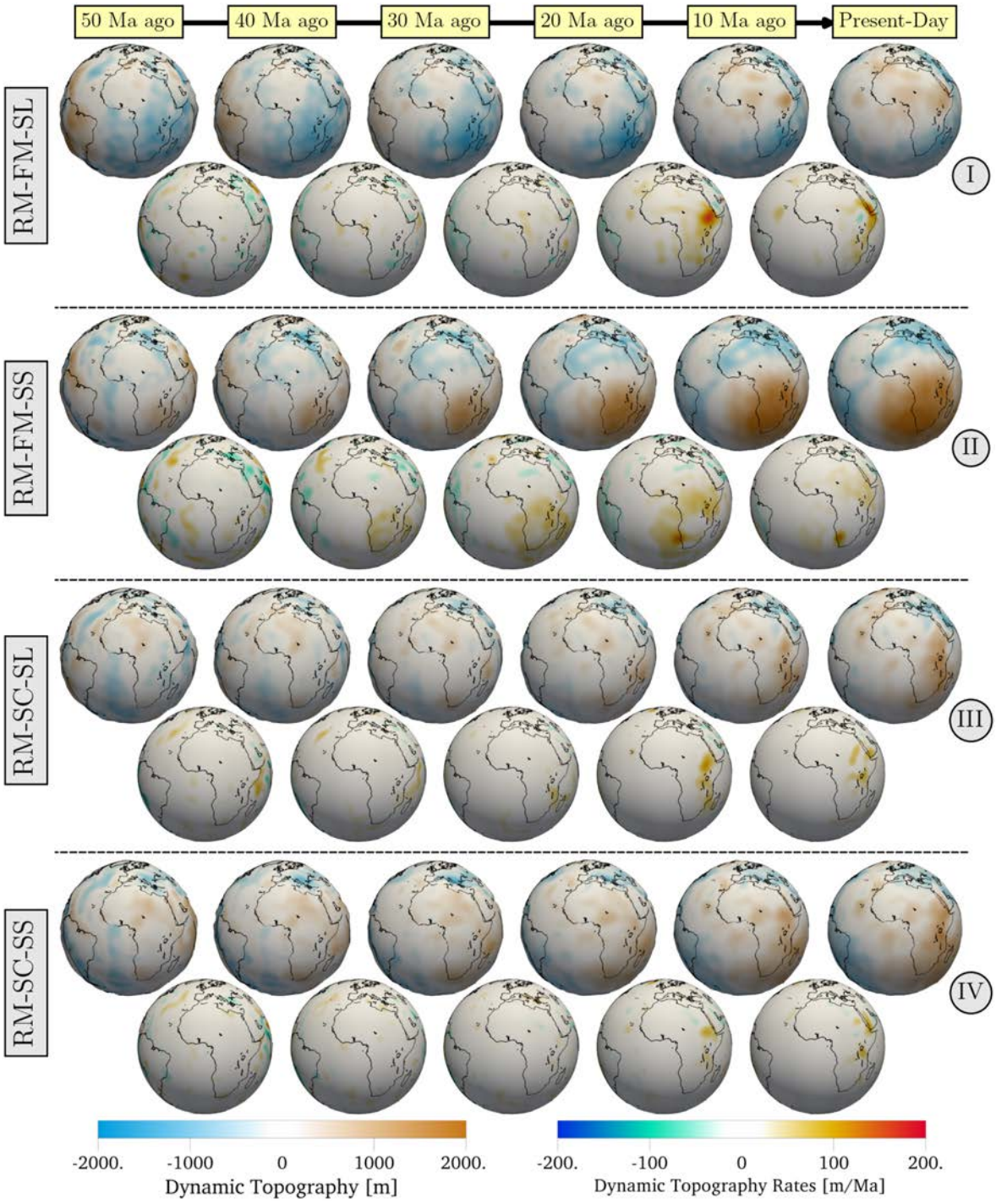

Figure 16. As in Fig. 8, but for in (I) MF-SL (SL2013sv and LLNL-G3D-JPS with MF-2004 profile), (II) MF-SS (SL2013sv and SEMUCB-WM1 with MF-2004 profile), (III) SC-SL (SL2013sv and LLNL-G3D-JPS with SC-2006 profile) and (IV) SC-SS (SL2013sv and SEMUCB-WM1 with SC-2006 profile). MF-SL retrodicts a low-standing African continent, followed by uplift in the North and along the East African Rift starting from 20 Ma with rates exceeding 200 m Myr^{-1}. MF-SS shows domal uplift over much of the southern part in the Cenozoic. SC-SL and SC-SS show broad agreement with MF-SL, with uplift signal along the East African Rift System.

Fig. 13). Our results agree with previous adjoint modelling of Spasojevic *et al.* (2009) for North America, although their use of a high viscosity layer (stress guide) in the upper mantle beneath the continent complicates a direct comparison of the dynamic topography evolution with their results. The retrodicted amplitude and rate of change in dynamic topography depend on the adopted viscosity profile. The stiffer μ_2 profile yields reduced amplitudes and rates of change, as expected from the dynamic topography kernels (Fig. 3). We also observe dynamic subsidence for the U.S. East coast since the Eocene, in agreement with earlier reports (Spasojevic *et al.* 2008). Importantly, none of the retrodictions generates an Oligo-Miocene growth of positive dynamic topography for the western United States, which is indicated by hiatus

surfaces (Hayek *et al.* 2020), so that the current topographic highstand of the western United States is absent from our models. The fact that the Yellowstone plume has been revealed only recently in greater detail by seismic models (Nelson & Grand 2018) provides a possible explanation for this result.

Looking at Australia next, we find again similar dynamic topography evolutions in our retrodictions. They are modulated in rate and amplitude by the assumed viscosity profile, as seen before for North America. In particular, all retrodictions develop a regional Cenozoic uplift signal for central and eastern Australia, in agreement with reports on the spatial and temporal patterns of Australian dynamic topography (e.g. Czarnota *et al.* 2014). The pattern coincides with long-wavelength northward tilting of the continent, which was emphasized by several authors (e.g. Sandiford 2007; DiCaprio *et al.* 2009). One type of geological evidence for Australia's northward tilting, as the continent moves towards the southeast Asia subduction systems, comes from high Miocene subsidence rates on the Australian northwest shelf, which are inferred from the stratigraphic architecture of carbonate platforms recording a switch from progradation to aggradation during Neogene times. The rapid subsidence exceeds passive-margin subsidence and seems to require a dynamic component (e.g. Czarnota *et al.* 2013; Rosleff-Soerensen *et al.* 2016). Importantly, the Australasian region illustrates the sensitivity of retrodictions to their tomographic input structure: models μ_1-SS and μ_2-SS generate a broad dynamic topography low in the early Cenozoic over much of Southeast Asia that gives way to regional uplift, while models μ_1-SL and μ_2-SL yield a broadly opposite trend, where a dynamic topography high in the early Cenozoic over much of Southeast Asia gives way to regional subsidence. The latter is consistent with reports on the absence of a Late Cretaceous–Eocene sedimentary record in Sundaland (Zahirovic *et al.* 2016).

Finally turning to Africa, we recall that the relationship of African topography to mantle flow processes was reviewed thoroughly by Burke & Gunnell (2008), while Şengör (2001) highlighted the response of East African and Arabian sedimentary systems to the rise of the Afar Plume. There have also been attempts to reconstruct the African landscape for much of the Cenozoic from river profiles (e.g. Paul *et al.* 2014) suggesting that the modern African topography developed since the Oligocene in response to mantle flow. Rapidly evolving sublithospheric processes beneath the continent are also indicated by the analysis of interregional Cenozoic hiatus surfaces (Carena *et al.* 2019). The latter show significant differences in spatial extent across Africa at the timescale of geological series (ten to a few tens of millions of years), much smaller than the mantle transit time (Iaffaldano & Bunge 2015). A strong expansion of total unconformable area at the base of the Miocene suggests that the Oligocene was a period of uplift in most of Africa. In southern Africa there is also a complete absence of marine sediments in both the Oligocene and Pleistocene, suggesting that southernmost Africa reached a high elevation in the Oligocene, subsided in the Miocene–Pliocene, and has been high again since the latest Pliocene or Pleistocene. Further detail on the analysis of hiatus surface in Africa is reported in Carena *et al.* (2019).

We recall as well that several recent geodynamic studies have modelled the Cenozoic dynamic topography evolution of Africa in response to mantle flow. From a variety of techniques that include backward advection (Moucha & Forte 2011), a back-and-forth iterative method for time-reversed convection (Faccenna *et al.* 2019) as well as adjoint modelling (Colli *et al.* 2018), these studies deduced that the current topographic highstand owes in part to the upwelling Afar plume, which is also seen in our models (Fig. 14). Our results broadly confirm these earlier studies, specifically for the weaker μ_1 profile. With this profile the retrodictions yield broad dynamic topography highs in the early Eocene, followed by subsidence in North Africa and uplift intensification in Eastern and Southern Africa, as hot material is drawn into the upwelling mantle beneath these regions. We note, however, that river profiles and hiatus surfaces are inconsistent with post Eocene subsidence in Northern Africa (Paul *et al.* 2014; Carena *et al.* 2019). Importantly the retrodictions reveal once more their sensitivity to the adopted viscosity profile. The stiffer lower mantle profile μ_2 yields nearly no positive dynamic topography for much of the Cenozoic, because much of the buoyant material is located at depth levels where their contribution is filtered out by the surface dynamic topography kernel (Fig. 3-III). Some uplift occurs in eastern Africa in the late Neogene, that is, the rise of the Afar plume is delayed in the high viscosity models.

The strong influence of the viscosity profile is also borne out in the retrodicted deep mantle flow histories. The μ_1 profile yields high flow velocities in the deep mantle, for instance under Africa, as material streams rapidly towards the upwelling regions beneath the continent. The flow velocities exceed 7 cm yr^{-1} in some regions, meaning they are difficult to reconcile with the existence of a hotspot reference frame (Duncan & Richards 1991). In other words, our retrodictions imply that deep mantle heterogeneities as imaged by LLNL-G3D-JPS and SEMUCB-WM1 are dynamically unstable under the assumption of the μ_1 profile and a purely thermal interpretation of seismic structure. To this end, a thermo-chemical interpretation of deep mantle structure (e.g. McNamara 2019) offers a plausible mechanism to yield reduced flow velocities. However, modest flow velocities with <3 cm yr^{-1} and greater stability of deep mantle heterogeneity for much of the retrodiction time occur for the μ_2 profile, so that a purely thermal interpretation of deep mantle heterogeneity (e.g. Schuberth *et al.* 2009b; Davies *et al.* 2012) is viable for the μ_2 profile. Further investigations are needed to test the competing compositional and rheological effects on the evolution of mantle flow retrodictions.

Retrodictions allow one to track material back in time from any given sampling point. This property makes them useful, for example, to geochemical studies. We focus on western Europe, because reports exist for this region of plume-like upper mantle seismic anomalies, for instance beneath the Eifel (Ritter *et al.* 2001), which cannot be linked easily to the lower mantle. In other words, the source location of these anomalies is poorly understood. Noting that there are differences in detail, we infer from Fig. 10 that all four end-member retrodictions imply that material currently located 120 km beneath the surface in western Europe was influxed from the Atlantic region in the west. While this would be consistent with geochemical reports (Hoernle *et al.* 1995), further analysis is needed to elucidate the upper mantle flow history beneath western Europe. A complex upper mantle flow history beneath Europe is also indicated by the retrodicted evolution of upper mantle velocities, shown in the top row of Fig. 11 for model μ_2-SL , which vary in space and time. Importantly, the retrodicted velocities exceed the

assimilated plate velocity in the lithosphere above, revealing a pressure driven (Poiseuille) flow component. We note that Höink & Lenardic (2010) explored the geodynamic implications of upper mantle flow in the context of Poiseuille/Couette flow and that Höink *et al.* (2011) predicted a Poiseuille flow regime for the Atlantic upper mantle from scaling analysis, consistent with our results. The upper mantle flow field in the Central Pacific, shown in the bottom row of Fig. 11 for model μ_2-SL , is also retrodicted as variable in space and time. The variations are triggered by the influx of warm material from the deeper sub-Pacific mantle. We note that they would impart a mantle wind that could affect the stability of hotspots over time (Tarduno *et al.* 2009). The horizontal stress field, shown in Fig. 12 for model μ_2-SL at a depth of 180 km, is in the range of a few MPa. This agrees with reports from global mantle flow studies (Steinberger *et al.* 2001; Kendall & Lithgow-Bertelloni 2016) and independent tectonic considerations on the stresses that drive plates from below (Bird *et al.* 2008). Importantly, the stress field is spatially coherent over distances >1000 km, so that it could integrate to tectonically relevant forces of $>10^{12}$ N m^{-1} .

We close our discussion by emphasizing the grave restrictions in our study. They severely limit the applicability of the current generation of global mantle flow retrodictions and make it plain that such models are still in their infancy. We recall that the accuracy of retrodictions strongly depends on the quality of key input information, including the present-day state estimate of the mantle as derived from seismic imaging, the rheological choices for the dynamic Earth model, as well as the assumptions on the thermal and compositional interpretation of seismic heterogeneity, all of which are subject to considerable uncertainty. Firstly, current tomographic models agree over length scales of thousands of km, but maintain differences at smaller scales (Becker & Boschi 2002; Shephard *et al.* 2017). So the use of different seismic state estimates implies different retrodicted flow histories, as seen in our study. Secondly, despite the range of radial viscosity profiles used in this study, we did not explore the effects of temperature and strain-rate (non-linear) viscosity variations. While the effects from radial viscosity variations likely exceed those from lateral variations (Tackley 1993), they influence the morphology of slabs and plumes (e.g. Whitehead & Luther 1975; Thompson & Tackley 1998; Bello *et al.* 2015) and their relative rising and sinking rates. This will need to be investigated in future retrodiction studies. Thirdly, we note that our analysis assumed no error in the surface velocity field, that is the past plate motion model, that is used over the assimilation period. In reality, our knowledge of past plate motions is not perfect, as noted before, even while substantial progress has been made (e.g. Müller *et al.* 2016). One may reduce measurement noise and improve the temporal resolution of relative plate motions via Bayesian analysis (Iaffaldano *et al.* 2012), but further assumptions, such as the choice of a reference frame, contribute to uncertainty in past plate motion models, especially as one goes further back in time (Shephard *et al.* 2012). Taken together this means that unavoidable limitations enter the retrodiction inverse problem in the form of poorly known model parameters and uncertain state estimations, resulting in systematic errors of the reconstructed flow history compared to the ideal case of no model error and no data error that was explored in early adjoint studies (e.g. Bunge *et al.* 2003). To explore the impact of model inconsistencies, Colli *et al.* (2020) recently performed a systematic study of these effects by analysing a series of synthetic adjoint inversions using purposefully mismatched model parameters. One conclusion drawn from their study is that it is not desirable to aim for a complete reduction of the cost function, as it results in overfitting. Such effects are generally avoided by imposing smoothness measures on the optimization problem. To this end, we have used two approaches: first, by low-pass filtering the misfit function to account for the difference between geodynamic and seismic model resolution, and secondly, by an early-stopping approach in which we explored the results after five iterations, as motivated by the findings from Colli *et al.* (2020). Such measures can be improved in future by representing the effects of seismic filtering by a resolution operator in case of the former (Ritsema *et al.* 2011; Simmons *et al.* 2019; Freissler *et al.* 2020), and explicit augmentations of the misfit function with a regularizing term in case of the latter (Li *et al.* 2017).

5 CONCLUSIONS

Mantle flow retrodictions are still in their infancy. But because they yield dynamic topography histories, they have the potential to link different observations and time scales in the solid Earth system, from geological to geodetic (Ghelichkhan *et al.* 2018, 2020), where they are sensitive to mantle flow induced vertical motions of the lithosphere. To this end, for the sake of simplicity we retrodicted the heterogeneity state of the Earth's mantle under a purely thermal interpretation since 50 Ma, applying the adjoint method in computationally demanding high resolution global geodynamic Earth models with $\approx$670 million finite elements and building upon our previous work presented by Colli *et al.* (2018). Specifically, we constructed a suite of eight retrodiction models from combinations of two different mantle state estimates derived from seismic imaging and four different mantle viscosity profiles, to acknowledge current uncertainties in our knowledge of large-scale mantle heterogeneity structure and first-order rheologic properties of dynamic Earth models. We compared the results from two end-member viscosity profiles μ_1 and μ_2 involving deep mantle viscosities of 1.7×10^{22} Pa s and 10^{23} Pa s, respectively, and two mantle state estimates against geological and geodynamic observations, including inferences of Cenozoic epeirogenic motion over North America, Australia and Africa. Importantly, we find the retrodictions and their associated dynamic topography histories are sensitive to the mantle state estimate and the radial viscosity profile of the Earth model, meaning that this input information is testable with inferences gleaned from the geological record and suggesting that retrodictions offer constraints on the underlying assumptions of dynamic Earth models. Our results imply that a purely thermal interpretation of deep mantle heterogeneities as imaged by Simmons *et al.* (2015) and French & Romanowicz (2015) is dynamically unstable under the assumption of the weaker μ_1 end-member viscosity profile. In this case lower mantle flow velocities exceed 7 cm yr^{-1} in some regions, meaning they are difficult to reconcile with the existence of a hotspot reference frame, whereas the μ_2 profile yields modest flow velocities (<3 cm yr^{-1}) and stability of deep mantle heterogeneity for much of the retrodiction time, albeit at the expense that African uplift is delayed into the latest Neogene, which conflicts with geological constraints. Retrodictions allow one to track material

back in time from any given sampling location. This makes them potentially useful, for example, to geochemical studies, for which we report examples from western Europe. Our results suggest that retrodictions may yield powerful synergies across different Earth sciences disciplines.

ACKNOWLEDGEMENTS

The authors are grateful to J.H. Davies and an anonymous reviewer for their constructive reviews and F. Simons for the editorial handling of the manuscript. A number of colleagues have helped with suggestions for the improvement of this material: G.F. Davies, D.R. Davies, B.S.A. Schuberth, M.J. Hoggard, P.W. Ball and L. Colli. The authors would like to thank the IT team at the Geophysics institute at LMU for their generous support during this project. SG is specially grateful to D.R. Davies for his support.

DATA AVAILABILITY

The 3-D rendering of the visualizations are done in Paraview software (Ahrens *et al.* 2005). For formatting of the figures and other type of visualizations, we have used Matplotlib (Hunter 2007) and Cartopy (Met Office 2010–2015). All the data and softwares in this study are properly referenced. Model results can be made available upon request.

REFERENCES

Ahrens, J., Geveci, B. & Law, C., 2005. Paraview: an end-user tool for large data visualization, *The Visualization Handbook,* Elsevier, ISBN-13: 978-0123875822.

Ammann, M., Brodholt, J., Wookey, J. & Dobson, D., 2010. First-principles constraints on diffusion in lower-mantle minerals and a weak d'' layer, *Nature,* **465**(7297), 462–465.

Andrault, D., Bolfan-Casanova, N., Nigro, G.L., Bouhifd, M.A., Garbarino, G. & Mezouar, M., 2011. Solidus and liquidus profiles of Chondritic mantle: implication for melting of the Earth across its history, *Earth planet. Sci. Lett.,* **304**(1), 251–259.

Ballmer, M.D., Schmerr, N.C., Nakagawa, T. & Ritsema, J., 2015. Compositional mantle layering revealed by slab stagnation at$\sim$ 1000-km depth, *Sci. Adv.,* **1**(11), e1500815.

Becker, T.W. & Boschi, L., 2002. A comparison of tomographic and geodynamic mantle models, *Geochem. Geophys. Geosyst.,* **3**(1), doi:10.129/2001GC000168.

Bello, L., Coltice, N., Rolf, T. & Tackley, P.J., 2014. On the predictability limit of convection models of the Earth's mantle, *Geochem. Geophys. Geosyst.,* **15,** 2319–2328.

Bello, L., Coltice, N., Tackley, P.J., Dietmar Mueller, R. & Cannon, J., 2015. Assessing the role of slab rheology in coupled plate-mantle convection models, *Earth planet. Sci. Lett.,* **430,** 191–201.

Bird, P., Liu, Z. & Rucker, W.K., 2008. Stresses that drive the plates from below: definitions, computational path, model optimization, and error analysis, *J. geophys. Res.,* **113**(B11), doi:10.1029/2007jb005460.

Bond, G., 1976. Evidence for continental subsidence in North America during the late cretaceous global submergence, *Geology,* **4**(9), 557–560.

Bond, G.C., 1978. Evidence for late Tertiary uplift of Africa relative to North America, South America, Australia and Europe, *J. Geol.,* **86**(1), 47–65.

Bozdağ, E., Peter, D., Lefebvre, M., Komatitsch, D., Tromp, J., Hill, J., Podhorszki, N. & Pugmire, D., 2016. Global adjoint tomography: first-generation model, *J. geophys. Int.,* **207**(3), 1739–1766.

Braun, J., 2010. The many surface expressions of mantle dynamics, *Nat. Geosci.,* **3**(12), 825–833.

Bunge, H.-P. & Baumgardner, J., 1995. Mantle convection modeling on parallel virtual machines, *Comp. Phys.,* **9,** 207–215.

Bunge, H.-P. & Davies, J.H., 2001. Tomographic images of a mantle circulation model, *Geophys. Res. Lett.,* **28**(1), 77–80.

Bunge, H.-P. & Glasmacher, U.A., 2018. Models and observations of vertical motion (MoveOn) associated with rifting to passive margins: preface, *Gondwana Res.,* **53,** 1–8.

Bunge, H.-P., Richards, M.A., Lithgow-Bertelloni, C., Baumgardner, J.R., Grand, S.P. & Romanowicz, B.A., 1998. Time scales and heterogeneous structure in geodynamic earth models, *Science,* **280**(5360), 91–95.

Bunge, H.-P., Hagelberg, C.R. & Travis, B.J., 2003. Mantle circulation models with variational data assimilation: inferring past mantle flow and structure from plate motion histories and seismic tomography, *J. geophys. Int.,* **152**(2), 280–301.

Burgess, P.M., Gurnis, M. & Moresi, L., 1997. Formation of sequences in the Cratonic interior of North America by interaction between mantle, Eustatic, and stratigraphic processes, *Bull. geol. Soc. Am.,* **109**(12), 1515–1535.

Burke, K. & Gunnell, Y., 2008. *The African Erosion Surface: A Continental-Scale Synthesis of Geomorphology, Tectonics, and Environmental Change Over the Past 180 Million Years*, Vol. **201,** Geological Society of America. doi:10.1130/2008.1201.

Butterworth, N.P., Talsma, A.S., Müller, R.D., Seton, M., Bunge, H.-P., Schuberth, B.S.A., Shephard, G.E. & Heine, C., 2014. Geological, tomographic, kinematic and geodynamic constraints on the dynamics of sinking slabs, *J. Geodyn.,* **73,** 1–13.

Cammarano, F., Goes, S., Vacher, P. & Giardini, D., 2003. Inferring upper-mantle temperatures from seismic velocities, *Phys. Earth planet. Inter.,* **138**(3), 197–222.

Cammarano, F., Goes, S., Deuss, A. & Giardini, D., 2005. Is a pyrolitic adiabatic mantle compatible with seismic data?, *Earth planet. Sci. Lett.,* **232**(3), 227–243.

Carena, S., Bunge, H.-P. & Friedrich, A.M., 2019. Analysis of geological hiatus surfaces across Africa in the Cenozoic and implications for the timescales of convectively-maintained topography, *Can. J. Earth Sci.,* **56**(12), 1333–1346.

Chust, T.C., Steinle-Neumann, G., Dolejš, D., Schuberth, B.S.A. & Bunge, H.-P., 2017. MMA-EoS: a computational framework for mineralogical thermodynamics, *J. geophys. Res.,* **122**(12), 9881–9920.

Colli, L., Stotz, I., Bunge, H.-P., Smethurst, M., Clark, S.R., Iaffaldano, G., Tassara, A., Guillocheau, F. & Bianchi, M.C., 2014. Rapid South Atlantic spreading changes and coeval vertical motion in surrounding continents: evidence for temporal changes of pressure-driven upper mantle flow, *Tectonics,* **33**(7), 1304–1321.

Colli, L., Bunge, H.-P. & Schuberth, B.S.A., 2015. On retrodictions of global mantle flow with assimilated surface velocities, *Geophys. Res. Lett.,* **42**(20), 8341–8348.

Colli, L., Ghelichkhan, S. & Bunge, H.-P., 2016. On the ratio of dynamic topography and gravity anomalies in a dynamic Earth, *Geophys. Res. Lett.,* **43**(6), 2510–2516.

Colli, L., Ghelichkhan, S., Bunge, H.-P. & Oeser, J., 2018. Retrodictions of mid paleogene mantle flow and dynamic topography in the atlantic region from compressible high resolution adjoint mantle convection models: Sensitivity to deep mantle viscosity and tomographic input model, *Gondwana Res.,* **53,** 252–272.

Colli, L., Bunge, H. & Oeser, J., 2020. Impact of model inconsistencies on reconstructions of past mantle flow obtained using the adjoint method, *J. geophys. Int.,* **221**(1), 617–639.

Connolly, J., 2005. Computation of phase equilibria by linear programming: a tool for geodynamic modeling and its application to subduction zone decarbonation, *Earth planet. Sci. Lett.,* **236**(1), 524–541.

Czarnota, K., Hoggard, M., White, N. & Winterbourne, J., 2013. Spatial and temporal patterns of cenozoic dynamic topography around Australia, *Geochem. Geophys. Geosyst.,* **14**(3), 634–658.

Czarnota, K., Roberts, G., White, N. & Fishwick, S., 2014. Spatial and temporal patterns of Australian dynamic topography from river profile modeling, *J. geophys. Res.,* **119**(2), 1384–1424.

Davaille, A. & Romanowicz, B., 2020. Deflating the LLSVPs: bundles of mantle thermochemical plumes rather than thick stagnant "piles", *Tectonics,* **39**(10),.

Davies, D.R., Goes, S., Davies, J.H., Schuberth, B.S.A., Bunge, H.-P. & Ritsema, J., 2012. Reconciling dynamic and seismic models of Earth's lower mantle: the dominant role of thermal heterogeneity, *Earth planet. Sci. Lett.,* **353–354**(0), 253–269.

Davies, D.R., Davies, J.H., Bollada, P.C., Hassan, O., Morgan, K. & Nithiarasu, P., 2013. A hierarchical mesh refinement technique for global 3-D spherical mantle convection modelling, *Geoscient. Model Dev.,* **6**(4), 1095–1107.

Davies, D.R., Goes, S. & Lau, H.C.P., 2015. *Thermally Dominated Deep Mantle LLSVPs: A Review,* pp. 441–477, Springer International Publishing, doi:10.1007/978-3-319-15627-9_14.

Davies, D.R., Valentine, A., Kramer, S.C., Rawlinson, N., Hoggard, M., Eakin, C. & Wilson, C., 2019. Earth's multi-scale topographic response to global mantle flow, *Nat. Geosci.,* **12**(10), 845–850.

Davies, G.F., 2009. Reconciling the geophysical and geochemical mantles: plume flows, heterogeneities, and disequilibrium, *Geochem. Geophys. Geosyst.,* **10**(10), doi:10.1029/2009GC002634.

Davies, G.F. & Richards, M.A., 1992. Mantle convection, *J. Geol.,* **100**(2), 151–206.

Debayle, E. & Ricard, Y., 2012. A global shear velocity model of the upper mantle from fundamental and higher Rayleigh mode measurements, *J. geophys. Res.,* **117**(10), 1–24.

Debayle, E., Dubuffet, F. & Durand, S., 2016. An automatically updated s-wave model of the upper mantle and the depth extent of azimuthal anisotropy, *Geophys. Res. Lett.,* **43**(2), 674–682.

DeMets, C., Gordon, R.G. & Argus, D.F., 2010. Geologically current plate motions, *J. geophys. Int.,* **181**(1), 1–80.

Deuss, A., 2009. Global observations of mantle discontinuities using SS and PP precursors, *Surv. Geophys.,* **30**(4–5), 301–326.

DiCaprio, L., Gurnis, M. & Müller, R.D., 2009. Long-wavelength tilting of the Australian continent since the late cretaceous, *Earth planet. Sci. Lett.,* **278**(3–4), 175–185.

Duncan, R.A. & Richards, M.A., 1991. Hotspots, mantle plumes, flood basalts, and true polar wander, *Rev. Geophys.,* **29**(1), 31–50.

Durand, S., Debayle, E., Ricard, Y., Zaroli, C. & Lambotte, S., 2017. Confirmation of a change in the global shear velocity pattern at around 1000 km depth, *J. geophys. Int.,* **211**(3), 1628–1639.

Dziewonski, A.M. & Anderson, D.L., 1981. Preliminary reference Earth model, *Phys. Earth planet. Inter.,* **25**(4), 297–356.

Şengör, A.M.C., 2001. Elevation as indicator of mantle-plume activity, in *Mantle Plumes: Their Identification Through Time,* Vol. **352,** pp. 183–245, eds Ernst, R.E & Buchan, K.L., Geological Society of America.

Ehlers, T.A. & Farley, K.A., 2003. Apatite (U–Th)/He thermochronometry: methods and applications to problems in tectonic and surface processes, *Earth planet. Sci. Lett.,* **206**(1–2), 1–14.

Faccenna, C., Glišović, P., Forte, A., Becker, T.W., Garzanti, E., Sembroni, A. & Gvirtzman, Z., 2019. Role of dynamic topography in sustaining the Nile River over 30 million years, *Nature Geoscience,* **12**(12), 1012–1017.

Fernandes, V.M. & Roberts, G.G., 2020. Cretaceous to recent net continental uplift from paleobiological data: insights into sub-plate support, *GSA Bull.,* doi:10.1130/b35739.1.

Fichtner, A., Kennett, B.L.N., Igel, H. & Bunge, H.-P., 2009. Full seismic waveform tomography for upper-mantle structure in the Australasian region using adjoint methods, *J. geophys. Int.,* **179**(3), 1703–1725.

Fichtner, A. *et al.*, 2018. The collaborative seismic earth model: generation 1, *Geophys. Res. Lett.,* **45**(9), 4007–4016.

Freissler, R., Zaroli, C., Lambotte, S. & Schuberth, B., 2020. Tomographic filtering via the generalized inverse: a way to account for seismic data uncertainty, *Geophys. J. Int.,* **223**(1), 254–269.

French, S.W. & Romanowicz, B.A., 2014. Whole-mantle radially anisotropic shear velocity structure from spectral-element waveform tomography, *J. geophys. Int.,* **199**(3), 1303–1327.

French, S.W. & Romanowicz, B.A., 2015. Broad plumes rooted at the base of the Earth's mantle beneath major hotspots, *Nature,* **525**(7567), 95–99.

Friedrich, A.M., Bunge, H.-P., Rieger, S.M., Colli, L., Ghelichkhan, S. & Nerlich, R., 2018. Stratigraphic framework for the plume mode of mantle convection and the analysis of interregional unconformities on geological maps, *Gondwana Res.,* **53,** 159–188.

Ghelichkhan, S. & Bunge, H.-P., 2016. The compressible adjoint equations in geodynamics: derivation and numerical assessment, *GEM-Int. J. Geomath.,* **7**(1), 1–30.

Ghelichkhan, S. & Bunge, H.-P., 2018. The adjoint equations for thermochemical compressible mantle convection: derivation and verification by twin experiments, *Proc. R. Soc., A,* **474**(2220), 20180329, doi:10.1098/rspa.2018.0329.

Ghelichkhan, S., Murböck, M., Colli, L., Pail, R. & Bunge, H.-P., 2018. On the observability of epeirogenic movement in current and future gravity missions, *Gondwana Res.,* **53,** 273–284.

Ghelichkhan, S., Fuentes, J.J., Hoggard, M.J., Richards, F.D. & Mitrovica, J.X., 2020. The precession constant and its long-term variation, *Icarus,* **358,** 114172, doi:10.1016/j.icarus.2020.114172.

Gordon, R.G. & Jurdy, D.M., 1986. Cenozoic global plate motions, *J. geophys. Res.,* **91**(B12), 12 389–12 406.

Guillocheau, F., Rouby, D., Robin, C., Helm, C., Rolland, N., Le Carlier de Veslud, C. & Braun, J., 2012. Quantification and causes of the terrigeneous sediment budget at the scale of a continental margin: a new method applied to the Namibia-South Africa margin, *Basin Res.,* **24**(1), 3–30.

Guillocheau, F., Simon, B., Baby, G., Bessin, P., Robin, C. & Dauteuil, O., 2018. Planation surfaces as a record of mantle dynamics: the case example of Africa, *Gondwana Res.,* **53,** 82–98..

Hager, B.H., Clayton, R.W., Richards, M.A., Comer, R.P. & Dziewonski, A.M., 1985. Lower mantle heterogeneity, dynamic topography and the geoid, *Nature,* **313**(6003), 541–545.

Hartley, R.A., Roberts, G.G., White, N.J. & Richardson, C., 2011. Transient convective uplift of an ancient buried landscape, *Nat. Geosci.,* **4**(8), 562–565.

Haskell, N., 1935. The motion of a viscous fluid under a surface load, *Physics,* **6**(8), 265–269.

Hayek, J.N., Vilacís, B., Bunge, H.-P., Friedrich, A.M., Carena, S. & Vibe, Y., 2020. Continent-scale hiatus maps for the Atlantic realm and Australia since the upper Jurassic and links to mantle flow induced dynamic topography, *Proc. R. Soc., A,* **476**(2242), 20200390, doi:10.1098/rspa.2020.0390.

Hirschmann, M.M., 2000. Mantle solidus: experimental constraints and the effects of peridotite composition, *Geochem. Geophys. Geosyst.,* **1**(10), doi:10.1029/2000GC000070.

Hoernle, K., Zhang, Y.-S. & Graham, D., 1995. Seismic and geochemical evidence for large-scale mantle upwelling beneath the eastern Atlantic and western and central Europe, *Nature,* **374**(6517), 34–39.

Hoggard, M., Austerman, J., Randel, C. & Stephenson, S., 2021. *Observing Dynamic Topography Through Space And Time,* AGU Geophysical Monograph 263. doi:10.1002/9781119528609.ch15.

Hoggard, M.J., White, N. & Al-Attar, D., 2016. Global dynamic topography observations reveal limited influence of large-scale mantle flow, *Nat. Geosci.,* **9,** 456–463.

Hoggard, M.J., Winterbourne, J., Czarnota, K. & White, N., 2017. Oceanic residual depth measurements, the plate cooling model, and global dynamic topography, *J. geophys. Res.,* **122**(3), 2328–2372.

Hoggard, M.J., Czarnota, K., Richards, F.D., Huston, D.L., Jaques, A.L. & Ghelichkhan, S., 2020. Global distribution of sediment-hosted metals controlled by Craton edge stability, *Nat. Geosci.,* **13**(7), 504–510.

Höink, T. & Lenardic, A., 2010. Long wavelength convection, Poiseuille-Couette flow in the low-viscosity asthenosphere and the strength of plate margins, *J. geophys. Int.,* **180**(1), 23–33.

Höink, T., Jellinek, A.M. & Lenardic, A., 2011. Viscous coupling at the lithosphere-asthenosphere boundary, *Geochem. Geophys. Geosyst.,* **12**(10), doi:10.1029/2011GC003698.

Horbach, A., Bunge, H.-P. & Oeser, J., 2014. The adjoint method in geodynamics: derivation from a general operator formulation and application to the initial condition problem in a high resolution mantle circulation model, *GEM: Int. J. Geomath.,* **5**(2), 163–194.

Hosseini, K., Sigloch, K., Tsekhmistrenko, M., Zaheri, A., Nissen-Meyer, T. & Igel, H., 2020. Global mantle structure from multifrequency tomography using P, PP and P-diffracted waves, *J. geophys. Int.,* **220**(1), 96–141.

Houser, C., Masters, G., Shearer, P. & Laske, G., 2008. Shear and compressional velocity models of the mantle from cluster analysis of long-period waveforms, *J. geophys. Int.,* **174**(1), 195–212.

Hunter, J.D., 2007. Matplotlib: a 2D graphics environment, *Comput. Sci. Eng.,* **9**(3), 90–95.

Iaffaldano, G. & Bunge, H.-P., 2015. Rapid plate motion variations through geological time: observations serving geodynamic interpretation, *Ann. Rev. Earth planet. Sci.,* **43,** 571–592.

Iaffaldano, G., Bodin, T. & Sambridge, M., 2012. Reconstructing plate-motion changes in the presence of finite-rotations noise, *Nat. Commun.,* **3,** 1048.

Ismail-Zadeh, A., Schubert, G., Tsepelev, I. & Korotkii, A., 2004. Inverse problem of thermal convection: numerical approach and application to mantle plume restoration, *Phys. Earth planet. Inter.,* **145**(1–4), 99–114.

Japsen, P., 2018. Sonic velocity of chalk, sandstone and marine shale controlled by effective stress: velocity-depth anomalies as a proxy for vertical movements, *Gondwana Res.,* **53,** 145–158.

Jarvis, G.T. & McKenzie, D.P., 1980. Convection in a compressible fluid with infinite Prandtl number, *J. Fluid Mech.,* **96**(03), 515–583.

Kendall, J.-M. & Lithgow-Bertelloni, C., 2016. Why is Africa rifting?, *Geol. Soc., Lond., Spec. Publ.,* **420**(1), 11–30.

Kennett, B.L.N. & Engdahl, E.R., 1991. Traveltimes for global earthquake location and phase identification, *J. geophys. Int.,* **105**(2), 429–465.

King, L.C., 1955. Pediplanation and isostasy: an example from South Africa, *Quart. J. Geol. Soc.,* **111**(1–4), 353–359.

Koelemeijer, P., Ritsema, J., Deuss, A. & Van Heijst, H.-J., 2016. Sp12rts: a degree-12 model of shear-and compressional-wave velocity for earth's mantle, *J. geophys. Int.,* **204**(2), 1024–1039.

Koelemeijer, P., Deuss, A. & Ritsema, J., 2017. Density structure of earth's lowermost mantle from Stoneley mode splitting observations, *Nat. Commun.,* **8**(1), 1–10.

Kohn, M.J., ed. 2007. *Paleoaltimetry: Geochemical and Thermodynamic Approaches*, Vol. 66 of Reviews in Mineralogy and Geochemistry, De Gruyter, doi:10.1515/9781501508608.

Krenkel, E., 1924. Die bruchzonen ostafrikas, *Geologische Rundschau,* **14**(3), 209–232.

Lei, W. *et al.*, 2020. Global adjoint tomography – model glad–m25, *J. geophys. Int.,* **223**(1), 1–21.

Li, D., Gurnis, M. & Stadler, G., 2017. Towards adjoint-based inversion of time-dependent mantle convection with nonlinear viscosity, *J. geophys. Int.,* **209**(1), 86–105.

Liu, C. & Grand, S.P., 2018. Seismic attenuation in the African LLSVP estimated from PCS phases, *Earth planet. Sci. Lett.,* **489,** 8–16.

Liu, L. & Gurnis, M., 2010. Dynamic subsidence and uplift of the Colorado plateau, *Geology,* **38**(7), 663–666.

Liu, L., Spasojević, S. & Gurnis, M., 2008. Reconstructing Farallon plate subduction beneath North America back to the late cretaceous, *Science,* **322**(5903), 934–938.

Lourens, L.J., Wehausen, R. & Brumsack, H.J., 2001. Geological constraints on tidal dissipation and dynamical ellipticity of the earth over the past three million years, *Nature,* **409**(6823), 1029–1033.

Lu, C., Grand, S.P., Lai, H. & Garnero, E.J., 2019. Tx2019slab: a new P and S tomography model incorporating subducting slabs, *J. geophys. Res.,* **124**(11), 11 549–11 567.

Lu, C., Forte, A.M., Simmons, N.A., Grand, S.P., Kajan, M., Lai, H. & Garnero, E., 2020. The sensitivity of joint inversions of seismic and geodynamic data to mantle viscosity, *Geochem. Geophys. Geosyst.,* **21**(4), e2019GC008648, doi:10.1029/2019GC008648.

Lyubetskaya, T. & Korenaga, J., 2007. Chemical composition of earth's primitive mantle and its variance: 2. Implications for global geodynamics, *J. geophys. Res.,* **112**(B3), doi:10.1029/2005jb004224.

Matthews, K.J., Hale, A.J., Gurnis, M., Müller, R.D. & DiCaprio, L., 2011. Dynamic subsidence of eastern Australia during the cretaceous, *Gondwana Res.,* **19**(2), 372–383.

McNamara, A.K., 2019. A review of large low shear velocity provinces and ultra low velocity zones, *Tectonophysics,* **760,** 199–220.

Mégnin, C., Bunge, H.-P., Romanowicz, B. & Richards, M.A., 1997. Imaging 3-D spherical convection models: what can seismic tomography tell us about mantle dynamics?, *Geophys. Res. Lett.,* **24**(11), 1299–1302.

Meinhold, G., 2010. Rutile and its applications in earth sciences, *Earth–Sci. Rev.,* **102**(1), 1–28.

Met Office, 2010-2015. *Cartopy: A Cartographic Python Library with a Matplotlib Interface*, Exeter, Devon.

Mitrovica, J. & Forte, A., 2004. A new inference of mantle viscosity based upon joint inversion of convection and glacial isostatic adjustment data, *Earth planet. Sci. Lett.,* **225**(1), 177–189.

Mitrovica, J.X., 1996. Haskell [1935] revisited, *J. geophys. Res.,* **101**(B1), 555.

Mitrovica, J.X., Beaumont, C. & Jarvis, G.T., 1989. Tilting of continental interiors by the dynamical effects of subduction, *Tectonics,* **8**(5), 1079–1094.

Montelli, R., Nolet, G., Dahlen, F. & Masters, G., 2006. A catalogue of deep mantle plumes: new results from finite-frequency tomography, *Geochem. Geophys. Geosyst.,* **7**(11), doi:10.1029/2006gc001248.

Morgan, W.J., 1968. Rises, trenches, great faults, and crustal blocks, *J. geophys. Res.,* **73**(6), 1959–1982.

Morrow, E., Mitrovica, J.X., Forte, A., Glišović, P. & Huybers, P., 2012. An enigma in estimates of the earth's dynamic ellipticity, *J. geophys. Int.,* **191**(3), 1129–1134.

Moucha, R. & Forte, A.M., 2011. Changes in African topography driven by mantle convection, *Nat. Geosci.,* **4**(10), 707–712.

Müller, R.D., Sdrolias, M., Gaina, C., Steinberger, B. & Heine, C., 2008. Long-term sea-level fluctuations driven by ocean basin dynamics, *Science,* **319**(5868), 1357–1362.

Müller, R.D. *et al.*, 2016. Ocean basin evolution and global-scale plate reorganization events since Pangea breakup, *Ann. Rev. Earth planet. Sci.,* **44**(1), 107–138.

Müller, R.D. *et al.*, 2018. Gplates: building a virtual earth through deep time, *Geochem. Geophys. Geosyst.,* **19**(7), 2243–2261.

Nakada, M. & Karato, S.-I., 2012. Low viscosity of the bottom of the earth's mantle inferred from the analysis of chandler wobble and tidal deformation, *Phys. Earth planet. Inter.,* **192,** 68–80.

Nakada, M. & Okuno, J., 2016. Inference of mantle viscosity for depth resolutions of GIA observations, *Geophys. Suppl. Mon. Not. R. Astron. Soc.,* **207**(2), 719–740.

Nakada, M., Okuno, J., Lambeck, K. & Purcell, A., 2015. Viscosity structure of Earth's mantle inferred from rotational variations due to GIA process and recent melting events, *J. geophys. Int.,* **202**(2), 976–992.

Nakiboglu, S., 1982. Hydrostatic theory of the earth and its mechanical implications, *Phys. Earth planet. Inter.,* **28**(4), 302–311.

Nelson, P.L. & Grand, S.P., 2018. Lower-mantle plume beneath the yellowstone hotspot revealed by core waves, *Nat. Geosci.,* **11**(4), 280–284.

Nerlich, R., Colli, L., Ghelichkhan, S., Schuberth, B. & Bunge, H.-P., 2016. Constraining central Neo-Tethys Ocean reconstructions with mantle convection models, *Geophys. Res. Lett.,* **43**(18), 9595–9603.

Obayashi, M., Yoshimitsu, J., Nolet, G., Fukao, Y., Shiobara, H., Sugioka, H., Miyamachi, H. & Gao, Y., 2013. Finite frequency whole mantle p wave tomography: improvement of subducted slab images, *Geophys. Res. Lett.,* **40**(21), 5652–5657.

Oeser, J., Bunge, H.-P. & Mohr, M., 2006. Cluster design in the Earth sciences: TETHYS, in *High Performance Computing and Communications. HPCC 2006. Lecture Notes in Computer Science*, Vol. 4208, pp. 31–40, Springer, doi:10.1007/11847366_4.

Pail, R. *et al.*, 2010. Combined satellite gravity field model GOCO01s derived from GOCE and GRACe, *Geophys. Res. Lett.,* **37**(20), doi:10.1029/2010GL044906.

Pälike, H. & Shackleton, N.J., 2000. Constraints on astronomical parameters from the geological record for the last 25 myr, *Earth planet. Sci. Lett.,* **182**(1), 1–14.

Panasyuk, S.V., Hager, B.H. & Forte, A.M., 1996. Understanding the effects of mantle compressibility on geoid kernels, *J. geophys. Int.,* **124**(1), 121–133.

Panning, M. & Romanowicz, B., 2006. A three-dimensional radially anisotropic model of shear velocity in the whole mantle, *J. geophys. Int.,* **167**(1), 361–379.

Paul, J.D., Roberts, G.G. & White, N., 2014. The African landscape through space and time, *Tectonics,* **33**(6), 898–935.

Paulson, A. & Richards, M.A., 2009. On the resolution of radial viscosity structure in modelling long-wavelength postglacial rebound data, *J. geophys. Int.,* **179**(3), 1516–1526.

Pekeris, C.L., 1935. Thermal convection in the interior of the earth, *J. geophys. Int.,* **3,** 343–367.

Piazzoni, A.S., Steinle-Neumann, G., Bunge, H.-P. & Dolejš, D., 2007. A mineralogical model for density and elasticity of the Earth's mantle, *Geochem. Geophys. Geosyst.,* **8**(11), doi:10.1029/2007GC001697.

Press, W.H., Teukolsky, S.A., Flannery, B.P. & Vetterling, W.T., 1992. *Numerical Recipes in Fortran 77: Volume 1, Volume 1 of Fortran Numerical Recipes: The Art of Scientific Computing,* Cambridge Univ. Press.

Price, M.G. & Davies, J.H., 2018. Profiling the robustness, efficiency and limits of the forward-adjoint method for 3D mantle convection modelling, *J. geophys. Int.,* **212**(2), 1450–1462.

Reali, R., Van Orman, J.A., Pigott, J.S., Jackson, J.M., Boioli, F., Carrez, P. & Cordier, P., 2019. The role of diffusion-driven pure climb creep on the rheology of Bridgmanite under lower mantle conditions, *Sci. Rep.,* **9,** 2045–2322.

Reuber, G.S. & Simons, F.J., 2020. Multi-physics adjoint modeling of earth structure: combining gravimetric, seismic, and geodynamic inversions, *GEM – Int. J. Geomath.,* **11,** doi:10.1007/s13137-020-00166-8.

Richards, F., Hoggard, M. & White, N., 2016. Cenozoic epeirogeny of the Indian peninsula, *Geochem. Geophys. Geosyst.,* **17**(12), 4920–4954.

Richards, F., Hoggard, M., Crosby, A., Ghelichkhan, S. & White, N., 2020a. Structure and dynamics of the oceanic lithosphere-asthenosphere system, *Phys. Earth planet. Inter.,* **309,** doi:10.1016/j.pepi.2020.106559.

Richards, F.D., Hoggard, M.J., White, N. & Ghelichkhan, S., 2020b. Quantifying the relationship between short-wavelength dynamic topography and thermomechanical structure of the upper mantle using calibrated parameterization of anelasticity, *J. geophys. Res.,* **125**(9), doi:10.1029/2019jb019062.

Richards, M.A. & Hager, B.H., 1984. Geoid anomalies in a dynamic Earth, *J. geophys. Res.,* **89**(B7), 5987.

Ringwood, A.E., 1991. Phase transformations and their bearing on the constitution and dynamics of the mantle, *Geochim. Cosmochim. Acta,* **55**(8), 2083–2110.

Ritsema, J., Deuss, A., van Heijst, H.J. & Woodhouse, J.H., 2011. S40RTS: a degree-40 shear-velocity model for the mantle from new Rayleigh wave dispersion, teleseismic traveltime and normal-mode splitting function measurements, *J. geophys. Int.,* **184**(3), 1223–1236.

Ritter, J.R., Jordan, M., Christensen, U.R. & Achauer, U., 2001. A mantle plume below the Eifel volcanic fields, Germany, *Earth planet. Sci. Lett.,* **186**(1), 7–14.

Roberts, G.G. & White, N., 2010. Estimating uplift rate histories from river profiles using African examples, *J. geophys. Res.,* **115**(B2), B02406.

Rosleff-Soerensen, B., Reuning, L., Back, S. & Kukla, P.A., 2016. The response of a basin-scale Miocene barrier reef system to long-term, strong subsidence on a passive continental margin, Barcoo sub-basin, Australian north west shelf, *Basin Res.,* **28**(1), 103–123.

Rowan, C.J. & Rowley, D.B., 2017. Preserved history of global mean spreading rate: 83 Ma to present, *J. geophys. Int.,* **208**(2), 1173–1183.

Rudolph, M.L., Lekić, V. & Lithgow-Bertelloni, C., 2015. Viscosity jump in earth's mid-mantle, *Science,* **350**(6266), 1349–1352.

Said, A., Moder, C., Clark, S. & Abdelmalak, M.M., 2015a. Sedimentary budgets of the Tanzania coastal basin and implications for uplift history of the east African rift system, *J. Afr. Earth Sci.,* **111,** 288–295.

Said, A., Moder, C., Clark, S. & Ghorbal, B., 2015b. Cretaceous-Cenozoic sedimentary budgets of the southern mozambique basin: implications for uplift history of the south African plateau, *J. Afr. Earth Sci.,* **109,** 1–10.

Sandiford, M., 2007. The tilting continent: a new constraint on the dynamic topographic field from Australia, *Earth planet. Sci. Lett.,* **261**(1–2), 152–163.

Schaber, K., Bunge, H.-P., Schuberth, B. S. A., Malservisi, R. & Horbach, A., 2009. Stability of the rotation axis in high-resolution mantle circulation models: weak polar wander despite strong core heating, *Geochem. Geophys. Geosyst.,* **10**(11), doi:10.1029/2009GC002541.

Schaeffer, A.J. & Lebedev, S., 2013. Global shear speed structure of the upper mantle and transition zone, *J. geophys. Int.,* **194**(1), 417–449.

Schuberth, B.S.A., Bunge, H.-P. & Ritsema, J., 2009a. Tomographic filtering of high-resolution mantle circulation models: can seismic heterogeneity be explained by temperature alone?, *Geochem. Geophys. Geosyst.,* **10**(5), Q05W03, doi:10.1029/2009GC002401

Schuberth, B.S.A., Bunge, H.-P., Steinle-Neumann, G., Moder, C. & Oeser, J., 2009b. Thermal versus elastic heterogeneity in high-resolution mantle circulation models with pyrolite composition: High plume excess temperatures in the lowermost mantle, *Geochem. Geophys. Geosyst.,* **10**(1), doi:10.1029/2008GC002235.

Schuberth, B.S.A., Zaroli, C. & Nolet, G., 2012. Synthetic seismograms for a synthetic Earth: long-period P- and S-wave traveltime variations can be explained by temperature alone, *J. geophys. Int.,* **188**(3), 1393–1412.

Shephard, G., Bunge, H.-P., Schuberth, B.S.A., Müller, R.D., Talsma, A.S., Moder, C. & Landgrebe, T.C.W., 2012. Testing absolute plate reference frames and the implications for the generation of geodynamic mantle heterogeneity structure, *Earth planet. Sci. Lett.,* **317–318,** 204–217.

Shephard, G.E., Müller, R.D., Liu, L. & Gurnis, M., 2010. Miocene drainage reversal of the Amazon River driven by plate–mantle interaction, *Nat. Geosci.,* **3**(12), 870–875.

Shephard, G.E., Matthews, K.J., Hosseini, K. & Domeier, M., 2017. On the consistency of seismically imaged lower mantle slabs, *Sci. Rep.,* **7**(1), 1–17.

Simmons, N.A., Forte, A.M. & Grand, S.P., 2009. Joint seismic, geodynamic and mineral physical constraints on three-dimensional mantle heterogeneity: implications for the relative importance of thermal versus compositional heterogeneity, *J. geophys. Int.,* **177**(3), 1284–1304.

Simmons, N.A., Forte, A.M., Boschi, L. & Grand, S.P., 2010. Gypsum: a joint tomographic model of mantle density and seismic wave speeds, *J. geophys. Res.,* **115**(B12), doi:10.1029/2010jb007631.

Simmons, N.A., Myers, S.C., Johannesson, G., Matzel, E. & Grand, S.P., 2015. Evidence for long-lived subduction of an ancient tectonic plate beneath the southern Indian Ocean, *Geophys. Res. Lett.,* **42**(21), 9270–9278.

Simmons, N.A., Schuberth, B.S.A., Myers, S.C. & Knapp, D.R., 2019. Resolution and covariance of the LLNL-G3D-JPS global seismic tomography model: applications to travel time uncertainty and tomographic filtering of geodynamic models, *J. geophys. Int.,* **217**(3), doi:10.1093/gji/ggz102.

Smith, A., Smith, D. & Funnel, B., 1994. *Atlas of Mesozoic and Cenozoic Landmasses,* Cambridge Univ. Press.

Spasojevic, S., Liu, L., Gurnis, M. & Müller, R.D., 2008. The case for dynamic subsidence of the U.S. east coast since the Eocene, *Geophys. Res. Lett.,* **35**(8), doi:10.1029/2008GL033511.

Spasojevic, S., Liu, L. & Gurnis, M., 2009. Adjoint models of mantle convection with seismic, plate motion, and stratigraphic constraints: North America since the late cretaceous, *Geochem. Geophys. Geosyst.,* **10**(5), doi:10.1029/2008gc002345.

Steinberger, B. & Calderwood, A.R., 2006. Models of large-scale viscous flow in the earth's mantle with constraints from mineral physics and surface observations, *J. geophys. Int.,* **167**(3), 1461–1481.

Steinberger, B. & O'Connell, R.J., 1997. Changes of the Earth's rotation axis owing to advection of mantle density heterogeneities, *Nature,* **387**(6629), 169–173.

Steinberger, B., Schmeling, H. & Marquart, G., 2001. Large-scale lithospheric stress field and topography induced by global mantle circulation, *Earth planet. Sci. Lett.,* **186**(1), 75–91.

Stephenson, S.N., White, N.J., Li, T. & Robinson, L.F., 2019. Disentangling interglacial sea level and global dynamic topography: analysis of madagascar, *Earth planet. Sci. Lett.,* **519,** 61–69.

Stixrude, L. & Lithgow-Bertelloni, C., 2005. Mineralogy and elasticity of the oceanic upper mantle: origin of the low-velocity zone, *J. geophys. Res.,* **110**(B3), doi:10.1029/2004JB002965.

Stixrude, L. & Lithgow-Bertelloni, C., 2011. Thermodynamics of mantle minerals - II. Phase equilibria, *J. geophys. Int.,* **184**(3), 1180–1213.

Tackley, P.J., 1993. Effects of strongly temperature-dependent viscosity on time-dependent, three-dimensional models of mantle convection, *Geophys. Res. Lett.,* **20**(20), 2187–2190.

Tape, C., Liu, Q., Maggi, A. & Tromp, J., 2009. Adjoint tomography of the southern California crust, *Science,* **325**(5943), 988–992.

Tappe, S., Budde, G., Stracke, A., Wilson, A. & Kleine, T., 2020. The tungsten-182 record of Kimberlites above the African Superplume: exploring links to the core-mantle boundary, *Earth planet. Sci. Lett.,* **547,** 116473.

Tarduno, J.A., Bunge, H.-P., Sleep, N.H. & Hansen, U., 2009. The bent Hawaiian-Emperor hotspot track: inheriting the mantle wind., *Science,* **324**(5923), 50–3.

Thompson, P.F. & Tackley, P.J., 1998. Generation of mega-plumes from the core-mantle boundary in a compressible mantle with temperature-dependent viscosity, *Geophys. Res. Lett.,* **25**(11), 1999–2002.

Thoraval, C. & Richards, M.A., 1997. The geoid constraint in global geodynamics: viscosity structure, mantle heterogeneity models and boundary conditions, *J. geophys. Int.,* **131**(1), 1–8.

Tikhonov, A.N., 1963. On the solution of ill-posed problems and the method of regularization, in *Doklady Akademii Nauk,* **151,** 501–504.

Tkalčić, H., Romanowicz, B. & Houy, N., 2002. Constraints on D" structure using PKP(AB-DF), PKP(BC-DF) and PcP-P traveltime data from broad-band records, *J. geophys. Int.,* **149**(3), 599–616.

Torsvik, T.H., Müller, R.D., Van Der Voo, R., Steinberger, B. & Gaina, C., 2008. Global plate motion frames: toward a unified model, *Rev. Geophys.,* **46**(3), RG3004.

Valentine, A.P. & Davies, D.R., 2020. Global models from sparse data: a robust estimate of earth's residual topography spectrum, *Geochem. Geophys. Geosyst.,* **21**(8), e2020GC009240, doi:10.1029/2020GC009240.

van Herwaarden, D.P., Boehm, C., Afanasiev, M., Thrastarson, S., Krischer, L., Trampert, J. & Fichtner, A., 2020. Accelerated full-waveform inversion using dynamic mini-batches, *J. geophys. Int.,* **221**(2), 1427–1438.

Vibe, Y., Friedrich, A.M., Bunge, H.-P. & Clark, S.R., 2018. Correlations of oceanic spreading rates and hiatus surface area in the North Atlantic realm, *Lithosphere,* **10**(5), 677–684.

Vynnytska, L. & Bunge, H., 2014. Restoring past mantle convection structure through fluid dynamic inverse theory: regularisation through surface velocity boundary conditions, *GEM - Int. J. Geomath.,* **6**(1), 83–100.

Weismüller, J., Gmeiner, B., Ghelichkhan, S., Huber, M., John, L., Wohlmuth, B., Rüde, U. & Bunge, H.-P., 2015. Fast asthenosphere motion in high-resolution global mantle flow models, *Geophys. Res. Lett.,* **42**(18), 7429–7435.

Whitehead, J.A.Jr & Luther, D.S., 1975. Dynamics of laboratory diapir and plume models, *J. geophys. Res.,* **80**(5), 705–717.

Wu, J. & Suppe, J., 2018. Proto-South China Sea Plate tectonics using subducted slab constraints from tomography, *J. Earth Sci.,* **29**(6), 1304–1318.

Wu, J., Suppe, J., Lu, R. & Kanda, R., 2016. Philippine Sea and East Asian plate tectonics since 52Ma constrained by new subducted slab reconstruction methods, *J. geophys. Res.,* **121,** 4670–4741.

Young, A., Flament, N., Maloney, K., Williams, S., Matthews, K., Zahirovic, S. & Müller, R.D., 2019. Global kinematics of tectonic plates and subduction zones since the late Paleozoic era, *Geosci. Front.,* **10**(3), 989–1013.

Zahirovic, S., Flament, N., Dietmar Müller, R., Seton, M. & Gurnis, M., 2016. Large fluctuations of shallow seas in low-lying southeast Asia driven by mantle flow, *Geochem. Geophys. Geosyst.,* **17**(9), 3589–3607.

Zaroli, C., 2016. Global seismic tomography using Backus–Gilbert inversion, *Geophys. Suppl. Mon. Not. R. Astron. Soc.,* **207**(2), 876–888.

Zaroli, C., Sambridge, M., Lévêque, J.-J., Debayle, E. & Nolet, G., 2013. An objective rationale for the choice of regularisation parameter with application to global multiple-frequency S-wave tomography, *Solid Earth,* **4**(2), 357–371.

Zhou, Q. & Liu, L., 2017. A hybrid approach to data assimilation for reconstructing the evolution of mantle dynamics, *Geochem. Geophys. Geosyst.,* **18**(11), 3854–3868.

Zindler, A. & Hart, S., 1986. Chemical geodynamics, *Ann. Rev. Earth Planet. Sci.,* **14,** 493–571.

APPENDIX

A1 Choices for lateral and radial filtering

Fig. A1 describes the filtering functions from eq. (2), and the choice of parameters.

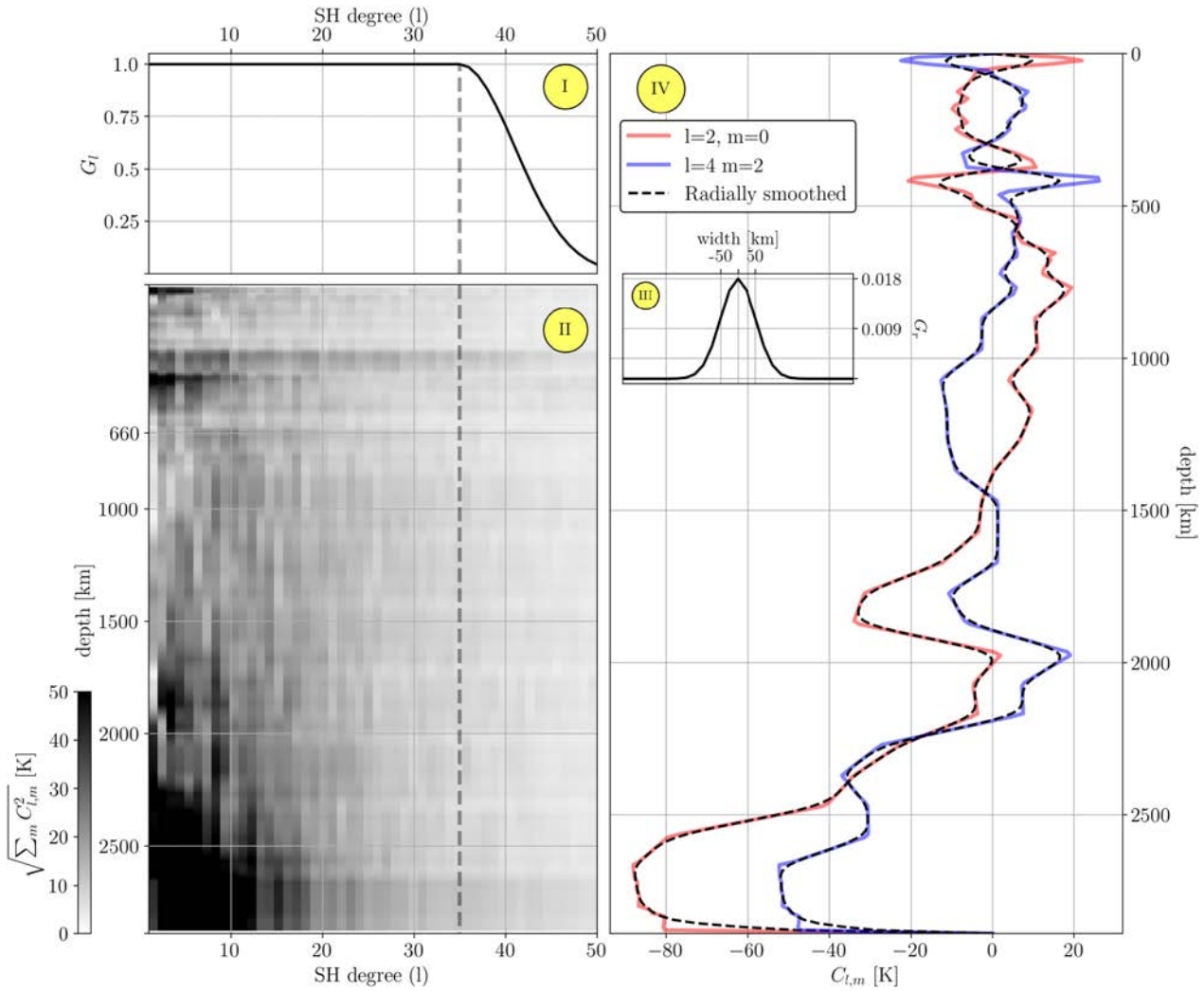

Figure A1. Functions for low-pass filtering of the misfit function in eq. (2), (I) G_l is 1 for all spherical harmonics less than $lmax = 35$ and tapers to zero at 50 with a Gaussian function. (II) square root of power spectrum for the unfiltered temperature field from LSQ_5P. $lmax = 35$ in (I) is chosen as the spherical harmonic degree that the amplitudes become significantly lower than in the longest wavelengths. (III) G_r, which is a normalized Gaussian function with the half-width of ≈50 km. (IV) radial filtering is achieved by convolution of G_r with radial profiles of spherical harmonics at each degree (l) and order (m). G_r in (III) is chosen such that it only prevents sharp radial gradient of temperatures at each wavelength, while it preserves the predicted temperature amplitudes from each model.